The influence of non-uniform ambient noise on crustal tomography in Europe

Piero Basini, Tarje Nissen-Meyer, Lapo Boschi, Emanuele Casarotti, Julie Verbeke, Olaf Schenk, Domenico Giardini

The influence of non-uniform ambient noise on crustal tomography in Europe

P. Basini[1],

T. Nissen-Meyer[2], L. Boschi[3],

E. Casarotti[4], J. Verbeke[5],

O. Schenk[6] and D. Giardini[2]

P. Basini, Department of Physics, University of Toronto, Toronto, Ontario, Canada M5S 1A7

L. Boschi, ISTEP, UMR 7193, UPMC Universite Paris 6, CNRS, FR-75005 Paris, France

E. Casarotti, INGV, via di Vigna Murata 605, 00143 Roma, Italy

D. Giardini, Institute of Geophysics, ETH Zurich, Sonneggstrasse 5, Zurich, Switzerland.

T. Nissen-Meyer, Institute of Geophysics, ETH Zurich, Sonneggstrasse 5, Zurich, Switzerland.

Olaf Schenk, Institute of Computational Science, University of Lugano, Via Giuseppe Buffi 13, Lugano, Switzerland.

J. Verbeke, Institute of Geophysics, Lamont-Doherty Earth Observatory, Columbia University, USA.

[1] Department of Physics, University of

Abstract. Ambient-noise seismology is of great relevance to high-resolution crustal imaging, thanks to the unprecedented dense data coverage it affords in regions of little seismicity. Under the assumption of uniformly distributed noise sources, it has been used to extract the Greens function between two receivers. We determine the imprint of this assumption by means of wave propagation and adjoint methods in realistic 3D Earth models. In this context, we quantify the sensitivity of ambient-noise cross correlations from central Europe with respect to noise-source locations and shear wavespeed structure.

Toronto, Toronto, Ontario, Canada M5S 1A7

[2]Institute of Geophysics, ETH Zurich, Sonneggstrasse 5, Zurich, Switzerland.

[3]ISTEP, UMR 7193, UPMC Universite Paris 6, CNRS, FR-75005 Paris, France

[4]INGV, via di Vigna Murata 605, 00143 Roma, Italy

[5]Lamont-Doherty Earth Observatory, Columbia University, USA

[6]Institute of Computational Science, University of Lugano, Via Giuseppe Buffi 13, Lugano, Switzerland.

We use ambient noise recorded over one year at 196 stations, resulting in a database of 864 cross-correlations. Our mesh is built upon a combined crustal and 3D tomographic model. We simulate synthetic ambient-noise cross-correlations in different frequency bands using a 3D spectral-element method. Traveltime cross-correlation measurements in these different frequency bands define the misfit between synthetics and observations as a basis to compute sensitivity kernels using the adjoint method. We perform a comprehensive analysis varying geographic station and noise-source distributions around the European seas. The deterministic sensitivity analysis allows for estimating where the starting crustal model shows better accordance with our dataset and gain insight into the distribution of noise sources in the European region. This highlights the potential importance to consider localized noise distributions for tomographic imaging and forms the basis of a tomographic inversion in which the distribution of noise sources may be treated as a free parameter similar to earthquake tomography.

1. Introduction

The European lithosphere is characterized by the presence of many microplates whose motion is dominated by convergence between Africa and Eurasia [e.g., *Schmid et al.*, 2004; *Boschi et al.*, 2010]. This results in the formation of strong 3D structural lateral variations which are difficult to image.

Nowadays, the majority of regional- and global-scale tomography models is based on the information obtained by either P- or S-wave traveltimes [*Bijwaard and Spakman*, 2000] or by surface-wave dispersion recorded from teleseismic events [*Chang et al.*, 2010; *Boschi et al.*, 2009; *Zhu et al.*, 2012]. While body waves are only partially sensitive to the structure of the crustal layers [*Schivardi and Morelli*, 2009], teleseismic surface waves are too rapidly attenuated to generate high-quality measurements at periods below 30 s [*Verbeke et al.*, 2012]. Resolution is further hampered by the strong non-uniformity in the source-receiver distribution [e.g. *Schaefer et al.*, 2011].

Ambient noise interferometry, applied in several different disciplines [*Aki*, 1957; *Cox*, 1973; *Duvall et al.*, 1993; *Shapiro et al.*, 2005], has been used to retrieve signals reminiscent of Green's functions between two receivers from the diffuse wavefield that receivers continuously record in the absence of earthquakes. It then becomes possible to compile large high-quality surface-wave databases and to perform surface wave tomography [e.g. *Shapiro and Campillo*, 2004; *Sabra et al.*, 2005; *Verbeke et al.*, 2012], wherever a dense station coverage exists.

Usually, seismic ambient-noise in the period-range 8-30 s considered in this work, shows two maxima in its spectrum between 10 and 20 s and between 5 and 10 s [e.g. *Stehly et al.*,

2006; *Yang et al.*, 2008]. *Hasselmann* [1963] relates the first maximum to the interaction of ocean swells with the shallow sea floor, while *Longuet-Higgins* [1950] identify the origin of the second one as the nonlinear interaction between ocean waves propagating in opposite directions.

The basic idea of ambient-noise seismology is the following: a cross-correlation recorded at two seismic stations (herafter correlogram as in [*Tanimoto*, 2008]) is produced by the interaction of waves equipartitioned in direction with random phases, and contains coherent signals that travel between the two stations. An often-made assumption postulates a uniform distribution of ambient noise sources surrounding the stations. This is however not valid in most regional-scale applications, as can easily be seen from correlograms consisting of a "causal" contribution, which contains the energy traveling from the station taken as the reference to the other, and an "anticausal" for the reverse case: causal and anticausal parts are symmetric with respect to the origin of the time axis only in presence of a diffuse wavefield. A diffuse wavefield can be generated if the noise sources are distributed uniformly or if scattering processes mimic the effect of this kind of distribution. However, at the frequencies we consider in this study, scattering is not expected to be sufficient to randomize wave propagation directions [*Paul et al.*, 2005]. Figure 1 shows that often (depending on configuration and properties of sources, scattering, absorption) the two branches of the correlograms present high asymmetry. *Stehly et al.* [2006], *Kedar et al.* [2008], *Landès et al.* [2010] and *Hillers et al.* [2012] show how the sources of ambient seismic noise, far from being uniform, are concentrated in the sea regions. In particular *Stehly et al.* [2006] verified, by analyzing the spectral bands corresponding to the primary (10-20 s) and the secondary (5-10 s) microseism for three different

datasets of ambient noise correlograms (North America, Africa and Europe), how the secondary microseism is related to the interaction of the ocean swell with the coastlines, while the primary microseism is related to ocean wave activity in deep water. *Snieder* [2004] suggests that source nonuniformity should not entirely compromise ambient-noise measurements of surface-wave velocity. However *Tsai and Moschetti* [2010] proved the importance of source distribution effects on surface-wave amplitudes and *Hanasoge* [2012] shows that the distribution of sources influences correlograms and how their knowledge is important to correctly interpret these data. *Mulargia* [2012] after analyzing from a statistical perspective the azimuthal isotropy of ambient-noise data recorded in various parts of the world, concludes that seismic noise wavefield is not generally diffuse.

The theoretical work of *Tromp et al.* [2010] (T10 hereafter) shows how adjoint techniques [e.g. *Tromp et al.*, 2005; *Peter et al.*, 2007] can be applied to ambient-noise seismology, taking into account the nonuniform distribution of noise sources. Our work represents one of the first applications of the adjoint methodology to a large, continental-scale set of high-quality ambient-noise correlograms in Europe [*Verbeke et al.*, 2012]. We shall highlight, in particular, the importance of properly defining the geographic distribution of noise sources, with the ultimate goal of improving on existing models of crust and uppermost mantle.

The paper is organized as follows: in Section 2 we describe the background model for our European study area based on new crustal and tomographic models and its discretization for 3D forward modeling. Section 3 describes the ambient-noise dataset gathered from this region of interest. In Section 4 we describe the different steps of the algorithm followed in this work; an Appendix offers a theoretical basis for the technique, largely based on

T10. Section 5 shows sensitivity kernels upon source location and wavespeed structure dependent on different starting models of the spatial distribution of noise sources, and different geographic distributions of seismic stations. From the analysis of the influence that these parameters have on the sensitivity kernels we can obtain a quantitative insight into the origin of ambient-noise and its effect on inversions for 3D structure.

2. Background model

Seismic waveform tomography aims at minimizing a misfit between synthetic and observed seismic waveform to improve the quality of the structural model used to compute synthetic data. Considering the crustal sensitivities of surface waves in the ambient-noise period range, we start with a tomographic 3D model to partially circumvent issues such as cycle skips or irretrievably disparate waveforms that may appear in simpler scenarios. The 3D velocity model used in this work combines a high-resolution European crustal model EPcrust [*Molinari and Morelli*, 2011] with an adaptive-resolution tomographic upper-mantle model FMADVOXEU′ [*Schaefer et al.*, 2011].

EPcrust is derived from the collection of several earlier, independent studies ([e.g. *Tesauro et al.*, 2008; *Grad and Tiira*, 2009; *Stehly et al.*, 2009]) based on active seismic experiments, surface-wave studies, noise correlation and receiver functions [*Molinari and Morelli*, 2011]. The model is parametrized in three layers: sediments, upper crust and lower crust. Within each layer, the model includes lateral variations of thickness and structure parameters (P- and S-wave speed, density).

FMADVOXEU′ is an adaptive-grid, anisotropic surface-wave tomography model of the uppermost mantle based on observations of Love- and Rayleigh-wave dispersion down to periods of 35 s [*Schaefer et al.*, 2011]. This model is defined globally with an adaptive-

voxel parametrization in which the size of each parametrization pixel depends on the data coverage at and around the pixel. This way, model resolution reflects data coverage, and the model's information content is optimized without over- and/or underparameterization. In particular, parametrization is denser over the European region, where data coverage is better. Starting from values of shear wavespeed β defined in the model, we derive values of compressional wave speed α and density ρ using the relation [*Karato*, 2003]:

$$R_{\beta/\alpha} \equiv \frac{\delta \log \beta}{\delta \log \alpha}, \tag{1}$$

and

$$R_{\rho/\beta,\alpha} \equiv \frac{\delta \log \rho}{\delta \log(\beta, \alpha)}, \tag{2}$$

where the variations of α and β are with respect to the PREM model and R has a value of 0.5. One of the most important factors affecting the accuracy of numerical wave propagation modelling is the construction of a high-quality mesh. The spectral-element package SPECFEM3D has the capability to incorporate fully unstructured hexahedral meshes [*Peter et al.*, 2011] using external meshers such as CUBIT [*Blacker et al.*, 1994], thus allowing for explicitely honoring all geological features (undulating Moho, surface topography) represented in models such as EPcrust.

We built a mesh that covers Europe and the surrounding oceans at latitudes between 30° and 65° north and longitudes between -46° and 47°, with horizontal dimensions of 3000×3000 km and a depth of 165 km. The mesh honors Earth's curvature and topography as well as lateral variations in Moho depth (figure 2 (b)) according to EPcrust. At the period range $8 - 30$ s considered in this work, surface waves have wavelength between 16 and 24 km, therefore, even if the topography is reproduced by the mesh, its effects will not be substantial in our simulations. The mesh is designed to simulate surface-

wave propagation at periods as low as 8 s, containing 192,892 elements for a total of 40,736,484 degrees of freedom. The maximum edge length of hexahedra is 24 km, but honoring the thickness of the crustal layer causes some regions to be characterized by elements with dimension of less than 10 km (figure 3). These small elements drive the stability condition of our simulations, leading to a numerical time step of 0.06 s. The sediment layer is neglected in areas where it is thinner than 1 km: given the dimension of the element edges, only the grid points on the free-surface of the mesh would sense these sediments, which would then not be relevant for the result of the simulations given our target resolution based on ambient noise spectra.

3. Cross-correlation measurements

We use a carefully processed dataset of vertical component ambient-noise correlograms from around Europe [*Verbeke et al.*, 2012]. This database has been obtained from one year of continuous seismic recording between January and December 2006 from the Swiss Network, the German Regional Seismological Network, the Italian national broad-band network and Orfeus. Using one year of data, seasonal effects associated with the geography of ocean storms are minimized [*Stehly et al.*, 2006]. Correlograms are computed following the approach described in *Bensen et al.* [2007], *Boschi et al.* [2012] and *Stehly et al.* [2006].

After rejecting station couples with relatively low signal-to-noise ratio, the database includes 864 correlogram observations. We measure the traveltime difference between observation-based and synthetic correlograms within time windows centered on surface waves, i.e. one per correlogram. Before performing this measurement we apply a bandpass Butterworth filter to both synthetics and data considering different period ranges: the upper bandpass limit is fixed at 30 s while the lower limit takes values of 10, 15 or 20 s.

Whenever the normalized cross-correlation between synthetic and data falls below 0.5, we ignore this measurement. Although this threshold value is low it is reasonable if we consider that (i) we are at the very first stage of the inversion process, (ii) the quality of the models used varies strongly within the area of study, (iii) considering such a wide area leads to a very high dispersion for surface waves so that an increase in the misfit is plausible. The number of measurements we could obtain for a given station dramatically decreased when considering period ranges with lower limits below 20 s. For example, our database contains a total of 45 observation-based ambient-noise correlograms for station AIGLE. Computing the traveltime misfit within the period band $20-30$ s we obtained a total of 24 measurements, but upon enlargening the period band down to 10 s, the number of acceptable measurements reduced to 15. This result was expected since EPcrust is best suited to reproduce signals with period between 20 and 30 s [*Molinari et al.*, 2012], and the tomographic model at even longer period.

In Figure 4, we show examples of comparison between observation-based and synthetic ambient-noise correlograms for two pairs of seismic stations. The comparison for station couple AIGLE-CEY might indicate that EPcrust is overall too slow with respect to real Earth structure in this area. Station couple ZUR-TNS on the contrary shows a very good agreement between synthetic and observation-based ambient-noise correlogram.

4. Computational procedure

T10 explain how the adjoint method [e.g., *Tromp et al.*, 2005; *Peter et al.*, 2007] can be applied in ambient-noise seismology to determine the sensitivity of noise correlograms to Earth and source properties, in particular for non-uniform distributions of noise-sources.

This study follows closely their formulation, of which we provide a summary in Appendix A.

We implement that procedure using the version 2.0 [*Peter et al.*, 2011] of the open-source spectral-element package SPECFEM3D. Appendix A shows that the procedure consists of three simulations per station. We describe them in the following and illustrate them for two sample stations in Fig. 5. Since this is, to the best of our knowledge, the first application of SPECFEM3D to spherical meshes, we benchmark our settings against the related code SPECFEM3D_GLOBE which is otherwise used for such settings, see Appendix B.

In general we assume for our settings that

1. ambient-noise is spatially uncorrelated (eq. A3);

2. the Peterson noise model [*Peterson*, 1993], filtered in the period window between 10 and 30 s, sufficiently describes the noise spectrum $|S(\omega)|$ around Europe;

3. we have a reliable initial guess of the geographic distribution of noise sources $\sigma(\mathbf{x})$.

A sensitivity analysis of the latter assumption is one of the crucial aspects of this paper. We select seismic station α as the "reference station" (green dot in figure 5). We then define a region at the free surface of our model in which we assume all the noise sources to be concentrated (grey dots in the bottom left panel of fig. 5). In the first simulation we compute the Green's tensor $\mathbf{G}(\mathbf{x}, \mathbf{x}^\alpha; t - t')$ upon a Dirac delta function at the location of the "reference" station. This result is then convolved with $|S_{ij}(\mathbf{x}, \omega)|$, derived from the ambient-noise spectrum, and we obtain the force F_i^α defined in equation (A12). We consider different period ranges for the spectrum (i.e. 10-30 s, 15-30 s and 20-30 s) in order to analyze the changes in the misfit between synthetic and observation-based ambient-

noise correlograms. We store the result of this first simulation at all points within the source region defined previously (see fig. 5 first column). The result of the first simulation is now used as forcing term in the second one, from which we obtain the wavefield $\mathbf{\Phi}^{\alpha}(\mathbf{x},\omega)$ of equation (A14 (second column of figure 5).

The cross-correlation traveltime difference acts as misfit between synthetic and observation-based ambient-noise correlograms:

$$\Delta T^{\alpha\beta} = T^{\alpha\beta}_{sim} - T^{\alpha\beta}_{obs}, \tag{3}$$

where $\Delta T^{\alpha\beta}$ relates to the stations pair $\alpha\beta$ (green and yellow dot in figure 5) and is determined by a cross-correlation of the synthetic and observation-based correlograms, for the same stations pair $T^{\alpha\beta}_{sim}$ and $T^{\alpha\beta}_{obs}$ denote the traveltime. Since both synthetic and observation-based ambient noise correlograms are dominated by surface waves, we measure the misfit only in the time-window corresponding to the arrival of these wave groups. For each synthetic correlogram, we select automatically the time window over which the traveltime difference is measured: the center of the interval is defined as the ratio of the distance between the station couple and the approximate minimum value of speed for Rayleigh waves. We select empirically for all the stations a fixed time-window width of 160 s, so that the whole signal associated with surface waves will be included in the misfit measurement.

The misfit is computed for each combination of reference and generic station, and following the same procedure used to obtain equation (A13) we define the adjoint sources for this kind of misfit as

$$\mathbf{F}^{\dagger\alpha\beta}(\mathbf{x},t) = -\frac{\hat{\nu}^{\beta}\Delta T^{\alpha\beta}\left\langle \dot{C}^{\alpha\beta}_{sim}\right\rangle(t)\delta(\mathbf{x}-\mathbf{x}^{\beta})}{\int\left[\left\langle \dot{C}^{\alpha\beta}_{sim}\right\rangle\right]^{2}}, \tag{4}$$

where $\hat{\nu}^{\beta}$ is the unit vector denoting the component of the station used for the correlogram.

We select 0.5 as the minimum value of the correlation coefficient between synthetic and observed data and we automatically reject all the couples synthetics-data that fall below this threshold. We next implement the sensitivity kernels implicit in equation (A16) by considering the causal and anticausal contributions separately. For the station couple $\alpha\beta$, this results in the "causal" kernel for density:

$$\left\langle K_{\rho}^{\alpha\beta} \right\rangle = -\int \rho \mathbf{\Phi}^{\dagger\alpha\beta}(-t) \cdot \partial_t^2 \mathbf{\Phi}^{\alpha}(t) \mathrm{d}t. \tag{5}$$

In the third and final simulation we inject the adjoint force defined in equation (4) at the position of station β (figure 5 third column, first panel). At the same time, we reconstruct the wavefield of the second simulation and the interaction of these two wavefields (figure 5 third column, second panel) described by equation (5) produces the "causal" sensitivity kernel for the density (figure 5 third column, third panel). The completion of the three simulations described above takes 1.3 h on 324 processors for one reference station. In order to perform a complete tomographic inversion, one needs to run this scenario for each reference station and iteration.

It is possible to define other types of kernels: for example in an isotropic Earth, we define the "causal" part of isotropic kernels for shear and bulk moduli respectively as

$$\left\langle K_{\mu}^{\alpha\beta} \right\rangle = -\int 2\mu \left[\mathbf{D}^{\dagger\alpha\beta}(-t) : \mathbf{D}^{\alpha}(t) \right] \mathrm{d}t, \tag{6}$$

$$\left\langle K_{\kappa}^{\alpha\beta} \right\rangle = -\int \kappa \left[\nabla \cdot \mathbf{\Phi}^{\dagger\alpha\beta}(-t) \nabla \mathbf{\Phi}^{\alpha}(t) \right] \mathrm{d}t, \tag{7}$$

where the traceless strain deviator and its adjoint are given by

$$\mathbf{D}^{\alpha} = \frac{1}{2} \left[\nabla \mathbf{\Phi}^{\alpha} + (\nabla \mathbf{\Phi}^{\alpha})^T \right] - \frac{1}{3} (\nabla \cdot \mathbf{\Phi}^{\alpha}) \mathbf{I}, \tag{8}$$

$$\mathbf{D}^{\dagger\alpha\beta} = \frac{1}{2} \left[\nabla \mathbf{\Phi}^{\dagger\alpha\beta} + (\nabla \mathbf{\Phi}^{\dagger\alpha\beta})^T) \right] - \frac{1}{3} (\nabla \cdot \mathbf{\Phi}^{\dagger\alpha\beta}) \mathbf{I}. \tag{9}$$

Using the two definitions of equation (6) it is possible to express the sensitivity kernels in terms of parameters such as the shear wave speed:

$$\left\langle K_{\beta}^{\alpha\beta} \right\rangle = 2 \left[\left\langle K_{\mu}^{\alpha\beta} \right\rangle - \frac{4}{3} \frac{\mu}{\kappa} \left\langle K_{\kappa}^{\alpha\beta} \right\rangle \right]. \tag{10}$$

Finally, we define the source kernel, that represents the sensitivity for the location of ambient noise sources, as the convolution between the adjoint wavefield $\mathbf{\Phi}^{\dagger\alpha\beta}$ and the forcing term F^{α} used in the second simulation:

$$\left\langle K_{\sigma}^{\alpha\beta} \right\rangle = \int \mathbf{\Phi}^{\dagger\alpha\beta}(-t) \cdot \mathbf{F}^{\alpha}(t) \mathrm{d}t. \tag{11}$$

Equations (5) - (11) can be obtained after some algebra from equation (A16).

The geographic distribution of noise sources $\sigma(\mathbf{x})$ is of fundamental importance in this process: it drives the wavefield $\Phi^{\alpha}(t)$ and thus both the synthetic ambient-noise correlograms and the sensitivity kernels are controlled by it.

The complete kernels, based on the ensemble correlogram $\left\langle C^{\alpha\beta} \right\rangle (t) = \left\langle C^{\beta\alpha} \right\rangle (-t)$, can be obtained by swapping α and β in these expressions and combining the results. In tomography applications, it is convenient to make use of the "misfit kernel" as defined by *Tape et al.* [2007]:

$$\langle K \rangle = \sum_{\alpha=1}^{N} \sum_{\beta \neq \alpha} \left\langle K^{\alpha\beta} \right\rangle \tag{12}$$

which corresponds to a cumulative cost function

$$\chi = \frac{1}{2} \sum_{\alpha=1}^{N} \sum_{\beta \neq \alpha} \Delta T^{\alpha\beta} \tag{13}$$

Once the misfit kernel is assembled, it is possible to compute the gradient of the misfit function $g_k = \int_{\Omega} K B_k \mathrm{d}^3\mathbf{x}$, where Ω is the model volume, K is the misfit kernel and B_k is a set of basis functions used to parametrize the model and on to which we project the misfit kernel. This gradient can then be used to update the initial structural model within the

framework of an iterative inversion. Before updating the model, a general smoothing of the misfit kernel is usually needed: depending on the period bandwith in which the misfit measurement is defined, artificial features may be introduced in the kernels as shown in *Tape et al.* [2010]. In this work we do not present any model update, so the plotted kernels are raw.

5. Noise sensivitity kernels

We next discuss the effect of the geographic distribution of noise sources on both source and shear-wavespeed sensitivity kernels. In practice, we repeat our kernel calculation three times, each time assuming noise sources to be limited to a certain area and homogeneously distributed across it, namely Baltic Sea, Mediterranean Sea, all sea/ocean areas. Note that the conventional assumption of a diffuse wavefield would imply placing the sources everywhere in the domain (oceanic and continental domains), thus possibly introducing even larger imprints compared to all of our allegedly more realistic choices. In earthquake-based seismology, individual source-receiver sensitivity kernels are obtained by the interaction of two distinct wavefields generated in two locations of the region of interest: an earthquake and a seismic station. At the latter location, the adjoint source must be placed to drive the "back-propagating" wavefield. A structural (e.g., wavespeed) kernel then illuminates the region comprised between the two points [*Peter et al.*, 2007] that is sensitive to structural scattering. In our case, the forward wavefields are driven by noise sources beyond the Fresnel zone of the two stations; we thus expect our region of sensitivity to significantly extend outside the area between the two seismic stations for this non-uniform source distribution.

It is important to clarify that sensitivity kernels are calculated based on a single-scattering approximation [*Zhou et al.*, 2011]. This may cause problems if the differences between recorded data and synthetics are large, and the effects caused by multiple scattering become important.

In the Introduction we identified the scattering as one of the processes needed to generate a diffuse wavefield. The exact role played by this factor has yet to be determined and is object of debate: as already mentioned, scattering, at the frequencies considered in this work is not sufficient to randomize wave propagation directions [*Paul et al.*, 2005]. *Campillo and Paul* [2003] point out the importance of scattering in the interferometric reconstruction of Green's functions examining the cross-correlation of late coda in earthquake data. On the contrary the experiments conducted by *Mikesell et al.* [2012] show how the reconstruction of the coda wave is less accurate compared to the reconstruction of the direct wave.

5.1. Sensitivity kernels for two-station couples

In this Section, we examine sensitivity kernels for two pairs of seismic stations, each covering a different area. Stations ARBF and KBA have a southwest-northeast azimuth, while AQU and SSY are oriented north-south. We chose these specific stations to analyze the effects of station azimuth on European noise sensitivity kernels. We simulate correlograms of ambient noise coming from all the sea regions, and define the misfit between these synthetic correlograms and our dataset as the cross-correlation traveltime difference measured on the causal branch.

We show in figure 6 (b) the β sensitivity kernel for the station couple ARBF-KBA: the sensitivity region covers not only the Alpine region but also the french Massif Central,

extending into the Cordillera Central in Spain. This high-sensitivity area protruding westward from station ARBF is presumably caused by the nonuniformity in the distribution of noise sources: if sources were distributed uniformly, the sensitivity kernel would be reminiscent of classic "banana-doughnuts" [T10, figure (5)]. Oscillations and changes of kernel values are probably caused by neglecting thin sediments as explained in Section 2, in fact figure 6 (c) represents the same K_β of panel (b) but at a depth of 30 km and it can be easily observed how the kernel at this depth is much smoother than above.

In figure 6 (d) we plot the source sensitivity kernel K_σ, for the same couple of stations: the area between the two seismic stations does not show any sensitivity. The two areas of sensitivity centered onto the seismic stations are different: the one pointing westward from ARBF is larger and shows higher values compared to the one centered in KBA. Also, the sensitivity region centered in ARBF does not have the same hyperbolic shape as the one centered on KBA, i.e. the low branch of the hyperbola that, based on the theoretical analysis of T10, one might expect to appear in the Mediterranean is missing. Another important feature is that the left lobe of the kernel presents a strong asymmetry towards the Biscay bay and the Atlantic ocean. These features are a direct consequence of the more effective interaction that the adjoint wavefield has with the forward wavefield coming from the Atlantic Ocean: these stations mostly record ambient noise coming from the Atlantic which is much noisier than the Mediterranean [*Stehly et al.*, 2006].

The geographic orientation of the AQU-SSY (figure 7 (a)) is almost orthogonal to ARBF-KBA, and roughly north-south. In this configuration, the two stations record synthetic ambient noise coming from the North Sea as well as from the Mediterranean: in this case, the assumption of uniform noise-sources distribution is presumably more

valid than for stations ARBF-KBA, in which the energy came primarly from the Atlantic Ocean. This is reflected also in the shape of the sensitivity kernels. At the free surface of our model (figure 7 (b)), the K_β sensitivity associated with AQU-SSY is concentrated between the two stations, in a small area around them and there is a prominent lobe of sensitivity centered on station AQU and pointing towards the Alps. The remarks about oscillations in K_β we made for ARBF-KBA are still valid, as shown by figure 7 (c). In this case K_σ (figure 7 (d)), shows a higher symmetry than in the previous configuration and it is possible to see the classic hyperbolic shape of the two "jets", departing from the two seismic stations [*Tromp et al.*, 2010].

5.2. Different Distribution of Noise Sources

In this Section we discuss sensitivity kernels obtained for a subset of selected 26 seismic stations, and for three different scenarios of ambient noise sources distributions. For each scenario we follow the method described in Appendix A: we consider each of the 26 stations respectively as the reference station, compute the sensitivity kernels for each reference station, and sum them together similar to summing event kernels as in *Tape et al.* [2007]. Our database of observation-based ambient-noise correlograms contains a different number of data for each station of reference, but sensitivity kernels are not comparable with those shown in the previous Section, since they result from the interaction of many singular kernels.

5.2.1. Baltic Sea

We first assume that all noise is generated in the Baltic Sea, i.e. the region covered by concentric grey circles in figure 8. Plots of K_σ in figure 8 (a) (b) and (c) show that certain stations then have a larger influence on the final results with respect to others: for

example we can see how kernel values obtained with ARSA as station of reference (figure 8 (a)) are larger than those obtained for stations such as ARCI or BSSO (respectively figures 8 (b) and (c)). We sum together all these single contributions in order to obtain the gradient of the misfit function. The result of this sum is shown in figure 8 (d), from which we can see how the source sensitivity kernels are largest along long and narrow strips pointing towards three distinct regions: the Mediterranean sea (particularly in the Adriatic), the Atlantic (particularly towards the coasts of Portugal and Bay of Biscay), and eastern Europe. This last result is partially in contrast with the assumption we made about the location of ambient noise sources, that is to say noise originates principally in the sea. From the analysis of the source sensitivity kernel K_σ for station ARSA, we can notice the presence of a strong jet of sensitivity pointing eastwards. Since station ARSA is located eastward with respect to the other stations used to build this kernel, it is straightforward to associate this result with this particular geographical position. The K_σ kernel associated with station BRANT, figure 9, shows a lobe of sensitivity pointing towards east, even if in this case the reference station is central with respect to the ones used to construct the sensitivity kernel.

5.2.2. Mediterranean

We next move the noise sources to the Mediterranean Sea (grey concentric circles in figure 10). All the inferences of Section 5.2.1 remain valid. K_σ, obtained as the sum of the single kernels for each station of reference (figure 10 (b)) shows lower values of sensitivity than in the previous case (figure 8 (d)), in particular, sensitivity decreases remarkably in the Adriatic Sea, suggesting that this region indeed produces ambient noise. Nevertheless we can still observe some jets protruding towards east.

Comparing the kernel obtained for the single station ARSA (figure 10 (a)) with the one obtained by positioning the sources of noise only in the Baltic Sea (figure 8 (a)), we find that the stations that most affect the sensitivity kernel are not the same as before; they are also fewer indicating that, neglecting ambient noise from the Baltic region, the misfit between synthetic correlograms and the observation-based ones increases. Yet even if the shape and the intensity of the kernel are different, the main direction of the sensitivity region still points towards east. The same behavior for the K_σ kernel can be found in the sensitivity kernel for station BRANT (figure 10 (c)).

5.2.3. Baltic + Mediterranean + Atlantic

In a third experiment, we choose all sea regions as noise sources in our starting model. If we look at the K_σ kernel, figure 11 (b), we can notice how the sensitivity towards the Atlantic and the one in the Mediterranean are almost reduced to zero, and we can see some jets pointing towards east. Let us analyze, as we did for the two previous cases, the source kernels for station ARSA and BRANT, respectively in figures 11 (a) and 11 (c). In the first one we can notice how the shape and the intensity of the kernel has changed once more: in particular there are some stations contributing to the kernel that did not appear in the previous cases. From the kernels for both stations it is clear how the sensitivity is pointing once more towards east. This result is in contradiction with the hypothesis of ambient noise generating exclusively in the sea, but it is not in contradiction with our dataset. If our assumption about the location of noise sources was correct then observation-based ambient noise correlograms for seismic stations like ARSA, which is the most eastward in our set, or BRANT should present values only in the branches representing energy traveling from west to east. Nevertheless if we analyze some of the

406 correlograms computed from recorded ambient noise for these two stations (figure 1), we
407 can clearly see how a significant portion of energy comes from the east.

408 From this set of experiments we can conclude that by distributing the noise sources in
409 all the sea regions, the source kernels are minimized, this indicating that this configuration
410 is, among those we analyzed, the most appropriate to describe the origin of ambient noise.
411 Nevertheless our data tell us that some energy is traveling from the east part of our region
412 of interest. This energy could represent ambient noise or it could indicate the presence of
413 a scatterer not reproduced by the structural model we are using in our simulations.

5.3. Shear wavespeed sensitivity

414 We now discuss K_β sensitivity kernels obtained for different configurations of noise-
415 source distributions as described previously.

416 5.3.1. Directional effects

417 In figure 12, we show three kernels for shear wavespeed constructed by summing 26
418 single contributions.

419 These three panels reveal some interesting observations about the importance of the
420 source distribution in ambient-noise tomography. All kernels show a sensitivity that is gen-
421 erally positive, indicating that the 3D shear background model is too slow. Further, they
422 exhibit a vague but characteristic dual stripe pattern between north and south. The top
423 panels (a) and (b) in figure 12 with noise originating from Baltic and Mediterranean Seas,
424 respectively, clearly feature more high-frequency contributions with oscillatory shapes
425 around the Alpine region than the all-encompassing kernel in (c). They also show an
426 elongated structure between stations and noise-source region, indicating that wavespeed
427 gradients tend to introduce a significant bias towards the (assumed-)source-receiver ge-

ometry. Figure 12 (c) shows noise in all surrounding seas, resulting in a smoother, multi-directional wavespeed kernel covering a larger continental area. This may of course simply be due to the same factor as above, i.e. reflecting the noise-source and station geometry. Assuming uniform coverage may therefore generally have the effect of smoothing gradients and further lead to a more pronounced coverage that seems less dependent on assumptions about the source location. At first glance, these effects may seem desirable from a tomographic perspective, but they do not necessarily reflect the true physical meaning if, as in most cases, noise sources are spatially localized as in panels (a) and (b) and thus lead to a potentially overemphasized kernel. Consequently, the consideration of non-uniform source distributions shall be considered carefully, and ideally in a joint-inversion framework.

5.3.2. Cumulative sensitivity

We now place noise sources in all the sea regions and compute shear wavespeed sensitivity kernels considering a total number of 104 "reference stations". Panels (a) and (b) of figure 13 show slices K_β computed for seismic stations ARSA and BRANT respectively and taken at a depth of 10 km. As in the case of K_σ (see figure 11) we notice that sensitivity is higher near station ARSA. This affects also both shape and values of the misfit kernel, figure 13 panel (c). In the case of station BRANT we notice a strong positive area of sensitivity around the Alpine region, as well a negative area extending from Switzerland to the northeast part of Germany.

The misfit kernel defined in Section 4 is obtained as the sum of all these 104 single contributions. The same negative area we found in figure 13 panel (b), can be identified also in this final misfit kernel reproduced in the same plot, panel (c). This indicates how in this region, differently from what happens in the rest of the study area, the model

451 we used has values of shear wavespeed too high. The final panel of figure 13 shows a
452 slice of the misfit kernel taken at a depth of 70 km. We notice how the sensitivity is
453 almost completely positive: this suggests that the velocity model at this depth needs to
454 be corrected with higher values of β. We are not expecting such monotone behaviour
455 during the whole inversion process: in the first iteration of their inversion *Tape et al.*
456 [2010] encountered a similar situation where the whole velocity model appeared to be
457 too fast but, after some iterations the kernels showed a more balance in sign. Panel (d)
458 of figure 13 shows how at 70 km depth the sensitivity areas become smoother and are
459 characterized by lower values with respect to those at 10 km depth (panel (c) of the same
460 figure): this is consistent with the fact that ambient noise comprises surface waves that
461 propagate within the uppermost 150 km.

462 These kernels are the basis for an iterative inversion by means of which it will be possible
463 to obtain a new tomographic image of Europe with much greater details than currently
464 available, thanks to the high frequencies in the noise data.

6. Conclusions

465 We presented ambient-noise source distributions as an integral part of a tomographic
466 inversion for crustal structure, and show the strong influence which a priori choices have
467 on wavespeed gradients, the building blocks for tomographic inversions. We use a dataset
468 of ambient-noise correlograms in central Europe [*Verbeke et al.*, 2012] and analyze the
469 sensitivity of noise-generated surface waves to 3D structure and the geographic distribu-
470 tion of the sources of ambient signal based on *Tromp et al.* [2010]. This framework allows
471 for nonuniform noise-source distributions, to account for the effects of nonuniformity in
472 noise-source distribution, which has not been possible in most ambient-noise tomography

literature so far. This is relevant to the problem of identifying the origin of ambient noise, closely related to the areas where noise comes from: for instance *Yang et al.* [2008] relate ambient noise to solid-earth-ocean coupling near coast, while *Stehly et al.* [2006] *Hillers et al.* [2012] and *Landès et al.* [2010] find thata it could also be generated by open-ocean processes. The workflow presented in Section 4 is general and can be applied to both local or global scale.

As a starting model, we use crustal model EPcrust [*Molinari and Morelli*, 2011] and a 3D tomographic model [*Schaefer et al.*, 2011] while honoring surface and Moho topography for down to a period of 8 s. We simulated synthetic ambient-noise correlograms and define a traveltime cross-correlation misfit between synthetics and data bandpass-filtered between 20 and 30 s. Using the adjoint method [*Tromp et al.*, 2005], we computed sensitivity kernels based on this misfit.

We analyzed the influence of stations distribution on sensitivity kernels, in particular we considered two couples with geographic orientation respectively north-south and east-west. The adjoint approach to tomography employed here requires that the geographic regions where ambient noise originates be known. We first treated all sea areas as noise sources, with a spectrum between 20 and 30 s described by the Peterson noise model [*Peterson*, 1993]. In both cases, β kernels are oscillatory at the free surface of the model, while at larger depth they become smoother. We interpreted this behavior as as consequence of not modeling the sediment layer in our numerical simulations, as explained in Section 2, in certain portions of the study area. The sensitivity kernels relating source strength, at a given location, to noise correlogram are characterized by very different patterns depending on azimuth: in the north-south configuration K_σ shows two symmetric jets departing from

the position of the two stations, while in the east-west configuration this symmetry is lost. The north-south pair is surrounded by the Adriatic and Mediterranean seas, resulting in noise sources being distributed rather symmetrically with respect to the receivers. The east-west pair, on the other hand, mostly records ambient noise coming from the Atlantic Sea, which is much "noisier" than the Mediterranean (see figures 6 and 7).

Finally we analyzed three different assumptions regarding the geographic distribution of noise sources, respectively we placed sources only in the Baltic Sea, only in the Mediterranean and in all the sea regions. For each scenario we consider 26 stations in turn as the station of reference, compute the sensitivity kernels for each reference station, and sum them together assembling the gradient of the misfit function. In the first case the source kernel showed high sensitivity in the Mediterranean and jets pointing towards the Atlantic Ocean and the east. In the second case we observed that it is not possible to ignore the noise coming from the Baltic Sea, since the number of stations that presented sufficiently low values of misfit decreased remarkably. In the third case the jets protruding towards the Atlantic disappeared and also the sensitivity in the Mediterranean decreased remarkably, but even in this case high-sensitivity areas protruding towards east were still present. This experiment indicates that the assumption of noise coming from all sea areas is the one closest to reality among those explored, since it minimizes the sensitivity kernel of the strength of the source: this means that structural perturbation to the starting model will be more effective, in fitting the data, with respect to source perturbation. This result is in accordance with what showed by *Stehly et al.* [2006]. However our dataset and the sensitivity kernels we computed showed that a certain amount of energy is generated to the east of our region of study. This energy could be related to the presence of noise

519 sources other than the ones located in the sea or to the presence of a scatterer not resolved
520 at present by the structural model used in this work.

521 The differences between the results obtained with different geographic distributions of
522 noise sources reveal how important this parameter is to tomographic imaging process, and
523 we infer that it should be treated as a free parameter in an iterative inversion. A possible
524 approach to this problem is to fix the noise sources distribution and after a certain number
525 of iterations validate the new velocity model using a set of independent data, for example
526 recorded from seismic events. Ambient-noise seismology, thanks to the unprecedentedly
527 dense data coverage it affords, is crucial to high-resolution crustal imaging, especially in
528 regions with limited earthquake coverage. Owing to the strong heterogeneity of the crust
529 leading to subsequent nonlinear effects in wave propagation, ambient-noise data should
530 be inverted in a full-wave based, iterative scheme such as the one proposed here. Besides
531 clarifying the influence of noise distributions, our sensitivity kernels drive an iterative
532 inversion, which will allow to obtain a new tomographic image of Europe with much
533 greater detail than currently available.

Appendix A: Outline of the theory

534 We start out with the equation of motion

$$\rho\partial_t^2\mathbf{s}(\mathbf{x},t) - \nabla\cdot[\mathbf{c}(\mathbf{x}) : \nabla\mathbf{s}(\mathbf{x},t)] = \mathbf{f}(\mathbf{x},t) \tag{A1}$$

536 [e.g., *Dahlen and Tromp*, 1998], where ρ denotes density, $\mathbf{x}$ location, t time, $\mathbf{s}$ displacement,
537 $\mathbf{c}$ the elastic tensor, and the forcing term $\mathbf{f}$ describes ambient-noise sources. We introduce
538 here an operator L such that eq. (A1) can also be written in the more compact form

$$L\mathbf{s}(\mathbf{x},t) = \mathbf{f}(\mathbf{x},t). \tag{A2}$$

In the assumption (typical for ambient-noise seismology) of spatially uncorrelated noise [e.g., *Boschi et al.*, 2012], the components $f_{1,2,3}$ of $\mathbf{f}$ have the property

$$\langle f_i(\mathbf{x}',\omega) f_j(\mathbf{x}'',\omega)\rangle = S_{ij}(\mathbf{x}',\omega)\delta(\mathbf{x}'-\mathbf{x}'') \quad (i=1,2,3; j=1,2,3), \tag{A3}$$

where ω is frequency, $\delta(\mathbf{x})$ the Dirac delta function, the tensor $\mathbf{S}$ describes the geographic and geometric properties and ω-dependence of the noise sources, and the operator $\langle ... \rangle$ stands for ensemble averaging. Ensemble averaging is the fundamental data-processing technique in all of ambient-noise seismology, allowing to reduce the effects of a set of sources and scatterers randomly distributed in space and time to those of a diffuse wavefield. It consists essentially of subdividing a long (e.g., one year) continuous seismic record into shorter intervals; whitening the records so that the effects of possible earthquake signals are minimized; cross-correlating simultaneous records from different stations, and finally stacking the results for each station pair over the entire year [e.g., *Bensen et al.*, 2007; *Boschi et al.*, 2012].

The approach of T10 is based on PDE-constrained optimization using Lagrange multipliers to find the extrema of a function $f(\mathbf{x})$, with $\mathbf{x}$ a vector of variables, subject to a condition $g(\mathbf{x}) = c$, with c a constant. The minimum and maximum values of Λ are achieved when the function $\Lambda(\mathbf{x},\lambda) = f(\mathbf{x}) + \lambda[g(\mathbf{x}) - c]$ is stationary, i.e. $\nabla_{\mathbf{x},\lambda}\Lambda = \mathbf{0}$. It is easy to see that this is in fact equivalent to $\nabla_{\mathbf{x},\lambda} f = \nabla_{\mathbf{x}} g$: in a 2-dimensional space, for instance, this equation is only satisfied at a location $\mathbf{x}$ where the curve $g(\mathbf{x}) = c$ is tangential to a contour line for the surface $f(\mathbf{x})$. For any pair of receivers α and β the function to be optimized (i.e. whose extrema are to be found) is the time-integrated difference:

$$\int \left[\Delta\langle C^{\alpha\beta}\rangle\right] \mathrm{d}t = \int \left[\langle C^{\alpha\beta}_{sim}\rangle - \langle C^{\alpha\beta}_{obs}\rangle\right]^2 \mathrm{d}t \tag{A4}$$

between the theoretical and observed ensemble correlograms $\langle C^{\alpha\beta}_{sim}\rangle$ and $\langle C^{\alpha\beta}_{obs}\rangle$, respectively. The condition (corresponding to $g(\mathbf{x}) = c$ above) is that the equation of motion (A1) be satisfied. This results in the requirement that the cost function χ, defined

$$\chi = \frac{1}{2}\int \left[\langle C^{\alpha\beta}_{sim}\rangle - \langle C^{\alpha\beta}_{obs}\rangle\right]^2 \mathrm{d}t - \langle \iint \boldsymbol{\lambda}\cdot(L\mathbf{s}-\mathbf{f})\,\mathrm{d}^3\mathbf{x}\mathrm{d}t\rangle, \tag{A5}$$

be minimum, consistent with eq. (19) of T10. Notice that, while the second term at the right-hand side of (A5) is defined by the physics of the medium of propagation, the first term represents one possible choice of the misfit function used to compare data and model predictions. The sensitivity functions obtained in the following depend on such choice, and if misfit is defined differently, sensitivity functions must be corrected accordingly.

The variables against which we optimize eq. (A5) are the components of the perturbation $\delta\mathbf{s}(\mathbf{x},t)$ to the displacement field. In their appendix A, T10 find an analytical expression for the variation

$$\begin{aligned}\delta\left\{\int\left[\Delta\langle C^{\alpha\beta}\rangle\right]^2\mathrm{d}t\right\} = \Big\langle\iint\Big[\hat{\nu}^\beta\int\Delta\langle C^{\alpha\beta}\rangle(\tau)s^\alpha(t+\tau)d\tau\delta(\mathbf{x}-\mathbf{x}^\beta)\\ + \hat{\nu}^\alpha\int\Delta\langle C^{\beta\alpha}\rangle(\tau)s^\beta(t+\tau)\delta(\mathbf{x}-\mathbf{x}^\alpha)\Big]\cdot\delta\mathbf{s}(\mathbf{x},t)d^3\mathbf{x}dt\Big\rangle\end{aligned} \tag{A6}$$

of the first integral at the right-hand side of (A5) caused by small perturbations $\delta\mathbf{s}(\mathbf{x},t)$. In their appendix B, they likewise find the variation of the second integral at the right-hand side of (A5) also resulting from $\delta\mathbf{s}(\mathbf{x},t)$. Both contributions to $\delta\chi$ are combined in an expression that we write compactly as

$$\begin{aligned}\delta\chi = \delta\left\{\int\left[\Delta\langle C^{\alpha\beta}\rangle\right]^2\mathrm{d}t\right\} + \iint\boldsymbol{\lambda}\cdot L\;\delta\mathbf{s}(\mathbf{x},t)\mathrm{d}t\mathrm{d}^3\mathbf{x}\\ + \iint\boldsymbol{\lambda}\cdot\delta L\;\mathbf{s}(\mathbf{x},t)\mathrm{d}t\mathrm{d}^3\mathbf{x} - \iint\boldsymbol{\lambda}\cdot\delta\mathbf{f}(\mathbf{x},t)\mathrm{d}t\mathrm{d}^3\mathbf{x}\end{aligned} \tag{A7}$$

(compare with eq. (B1) of T10). In the case of no medium and source perturbations, eq. (A7) is reduced to

$$\delta\chi = \delta\left\{\int\left[\Delta\langle C^{\alpha\beta}\rangle\right]^2\mathrm{d}t\right\} + \iint\boldsymbol{\lambda}\cdot L\;\delta\mathbf{s}(\mathbf{x},t)\mathrm{d}t\mathrm{d}^3\mathbf{x}. \tag{A8}$$

Through the integration by parts of terms involving spatial and temporal derivatives of $\mathbf{s}$ and $\delta\mathbf{s}$, this can be rewritten

$$\delta\chi = \delta\left\{\int \left[\Delta\langle C^{\alpha\beta}\rangle\right]^2 \mathrm{d}t\right\} - \iint \delta\mathbf{s}\cdot L\,\boldsymbol{\lambda}\,\mathrm{d}t\mathrm{d}^3\mathbf{x}. \tag{A9}$$

After replacing $\delta\left\{\int \left[\Delta\langle C^{\alpha\beta}\rangle\right]^2 \mathrm{d}t\right\}$ with its expression (A6), and the algebra carried out by T10 in their Appendix B, it follows from eq. (A9) that the variation (A8) is stationary ($\delta\chi = 0$) if the multiplier $\boldsymbol{\lambda}$ satisfies

$$L\boldsymbol{\lambda} = \mathbf{f}^\dagger \tag{A10}$$

equivalent to eq. (B6) of T10, with the right-hand side $\mathbf{f}^\dagger$ given by eq. (B7) of T10. Importantly $\mathbf{f}^\dagger$ contains the variation $\delta\left\{\int \left[\Delta\langle C^{\alpha\beta}\rangle\right]^2 \mathrm{d}t\right\}$, and hence the observation $\langle C^{\alpha\beta}_{obs}\rangle$. Comparing (A10) with (A2), $\mathbf{f}^\dagger$ is naturally interpreted as a forcing term (a source). Let us dub it "adjoint source". The solution $\boldsymbol{\lambda}$ to (A10) is the corresponding displacement field, or the "adjoint wavefield", which is usually denoted $\mathbf{s}^\dagger$.

Let us now perturb the parameters describing the medium of propagation (density, elastic tensor), and the source term $\mathbf{f}$. We substitute $\boldsymbol{\lambda}$ with $\mathbf{s}^\dagger$ in eq. (A7); since $\mathbf{s}^\dagger$ is a solution to (A10), we find

$$\delta\chi = -\frac{1}{2\pi}\left\langle \iint \left(-\omega^2\delta\rho\mathbf{s}^\dagger\cdot\mathbf{s} + \nabla\mathbf{s}^\dagger : \delta\mathbf{c} : \nabla\mathbf{s} - \mathbf{s}^\dagger\cdot\delta\mathbf{f}\right)\mathrm{d}^3\mathbf{x}\mathrm{d}\omega \right\rangle, \tag{A11}$$

equivalent to eq. (C1) of T10.

In their Appendix C, T10 manipulate eq. (A11) to show how ambient-noise sensitiviy kernels for any given station pair can be calculated with three spectral-element simulations only. They start by substituting $\mathbf{s}$ in (A11) with the convolution of the Green's function $\mathbf{G}$ and the forcing term $\mathbf{f}$, and likewise $\mathbf{s}^\dagger$ with the convolution of $\mathbf{G}$ and $\mathbf{s}^\dagger$. The resulting expression (eq. (C4) in T10) involves the products $f_i^*(\mathbf{x},\omega)f_j(\mathbf{x}',\omega)$, $f_i^*(\mathbf{x},\omega)\delta f_j(\mathbf{x}',\omega)$

which we know from (A3) to coincide, in the assumption of spatially uncorrelated noise, with $S_{ij}(\mathbf{x},\omega)\delta(\mathbf{x}-\mathbf{x}')$ and $\delta S_{ij}(\mathbf{x},\omega)\delta(\mathbf{x}-\mathbf{x}')$, respectively. The integrals are accordingly simplified, resulting in the (still very cumbersome) eq. (C5) of T10, where a more compact form for that equation is obtained by introducing the "sources" (eqs. (C7) and (C10))

$$F_i^\alpha(\mathbf{x},\omega) = G_{jk}^*(\mathbf{x},\mathbf{x}^\alpha;\omega)\nu_k^\alpha S_{ij}(\mathbf{x},\omega), \tag{A12}$$

$$\mathbf{F}^{\dagger\alpha\beta}(\mathbf{x},\omega) = \hat{\nu}^\beta \Delta\langle C\rangle^{\alpha\beta}(\omega)\delta(\mathbf{x}-\mathbf{x}^\beta), \tag{A13}$$

with associated wavefields (eqs. (C8) and (C11) of T10)

$$\mathbf{\Phi}^\alpha(\mathbf{x},\omega) = \int_V \mathbf{G}(\mathbf{x},\mathbf{x}';\omega)\cdot\mathbf{F}^\alpha(\mathbf{x}',\omega)\mathrm{d}^3\mathbf{x}', \tag{A14}$$

$$\mathbf{\Phi}^{\dagger\alpha\beta}(\mathbf{x},\omega) = \int_V \mathbf{G}(\mathbf{x},\mathbf{x}';\omega)\cdot\mathbf{F}^{\dagger\alpha\beta}(\mathbf{x}',\omega)\mathrm{d}^3\mathbf{x}'. \tag{A15}$$

Substituting $\mathbf{F}^{\dagger\alpha\beta}$, $\mathbf{F}^\alpha$, $\mathbf{\Phi}^\alpha$ and $\mathbf{\Phi}^{\dagger\alpha\beta}$ into their eq. (C5) for the variation $\delta\chi$, T10 find the following compact expression

$$\begin{aligned}\delta\chi = &-\frac{1}{2\pi}\iint\left[-\omega^2\delta\rho\left(\Phi_i^{\dagger\alpha\beta}\Phi_i^\alpha + \Phi_i^{\dagger\beta\alpha}\Phi_i^\beta\right) + \delta c_{ijkl}\left(\nabla_i\Phi_j^{\dagger\alpha\beta}\nabla_k\Phi_l^\alpha + \nabla_i\Phi_j^{\dagger\beta\alpha}\nabla_k\Phi_l^\beta\right)\right]\mathrm{d}^3\mathbf{x}\mathrm{d}\omega \\ &+\frac{1}{2\pi}\iint\left(\Phi_i^{\dagger\alpha\beta}\delta F_i^\alpha + \Phi_i^{\dagger\beta\alpha}\delta F_i^\beta\right)\mathrm{d}^3\mathbf{x}\mathrm{d}\omega,\end{aligned} \tag{A16}$$

where $\delta F_i^\alpha(\mathbf{x},\omega) = G_{jk}^*(\mathbf{x},\mathbf{x}^\alpha;\omega)\nu_k^\alpha\delta S_{ij}(\mathbf{x},\omega)$. It should be clear that the factors multiplying $\delta\rho$, δc_{ijkl} and the combination of adjoint wavefield $\mathbf{\Phi}^\dagger$ with the variation of the force $\delta\mathbf{F}$ in (A16) are nothing but the partial derivatives (sensitivity kernels) relating our cost function to variations in the model parameters (density and elastic tensor) and source properties, which will be the unknowns of our inverse problem.

Now, in the same spirit as, e.g., *Peter et al.* [2007], the convolution of a Green's function with any source term can be interpreted as the result of injecting said source term in a numerical integration algorithm, like, in our case, the spectral element software of *Tromp*

et al. [2008], and computing the associated wavefield. Inspection of eq. (A16) shows that three simulations are needed to identify all quantities in (A16) except for the unknown perturbations in structure and source parameters. We must first compute the response of our model to an impulsive perturbation at the receiver location $\mathbf{x}^\alpha$, i.e. $\mathbf{G}(\mathbf{x}, \mathbf{x}^\alpha; \omega)$, to be then filtered by $\mathbf{S}(\mathbf{x}, \omega)$ at all locations $\mathbf{x}$: this gives us the forcing term (A12). We next (second simulation) simulate the effects of the forcing (A12), equivalent to expression (A14). Finally, a third simulation is likewise associated with eqs. (A13) and (A15). These correspond, respectively, to the first, second and third simulations introduced in Section 4.

Appendix B: Validation of the spherical mesh

The mesh we built for our application covers a region that reaches from Greece to the Atlantic Ocean (coasts of Greenland) and from Sicily to the northern Scandinavian Peninsula. Thus, the mesh takes into account the curvature of the Earth and is made by a set of spherical shells portions on which we superimpose the geometry of both Earth's topography and Moho. To our knowledge, this application is the first that uses the code SPECFEM3D version 2.0 with spherical meshes, thus we decided to benchmark the code against the version SPECFEM3D_GLOBE. To test the stability of our mesh we have placed a cross-shaped array of seismic receivers on the free surface of the mesh. The distance between each station is about 100 km. We have simulated a 10 km deep explosion located exactly at the center of the array, with a characteristic period of 10 s. We have performed the same experiment using the SPECFEM3D_GLOBE version of the code, which uses an internal mesher. Result of this benchmark are shown in figure 14. We applied to the synthetic a bandpass Butterworth filter between 10 and 30 s in order

to eliminate all the possible numerical noise. This period range is the same in which the synthetic noise used in our application is defined. The comparison of results obtained with the two different codes shows a good agreement both in terms signal phases and amplitudes.

Acknowledgments.

This work greatly benefitted from discussions with J. Tromp, D. Peter, and S. Hanasoge and from the comments of the two reviewers C. Tape and G. Hillers. This work has been supported by the European Marie-Curie initial training network QUEST and the Swiss HP2C platform project "Petaquake". Simulations were undertaken at the Swiss National Supercomputing Center, whose support is greatly appreciated.

References

Aki, K. (1957), Space and time spectra of stationary stochastic waves, with special reference to microtremors, *B. Earthq. Res. I Tokyo*, *35*(3), 415–456.

Bensen, G. D., M. H. Ritzwoller, M. P. Barmin, A. L. Levshin, F. Lin, M. P. Moschetti, N. M. Shapiro, and Y. Yang (2007), Processing seismic ambient noise data to obtain reliable broad-band surface wave dispersion measurements, *Geophys. J. Int.*, *169*(3), 1239–1260, doi:10.1111/j.1365-246X.2007.03374.x.

Bijwaard, H., and W. Spakman (2000), Non-linear global P-wave tomography by iterated linearized inversion, *Geophys. J. Int.*, *141*(1), 71–82, doi:10.1046/j.1365-246X.2000.00053.x.

Blacker, T. D., W. J. Bohnho, and T. L. Edwards (1994), *CUBIT mesh generation environment. Volume 1: Users manual*, Sandia National Labs., Albuquerque, NM (United

States), doi:10.2172/10176386.

Boschi, L., B. Fry, G. Ekström, and D. Giardini (2009), The European Upper Mantle as Seen by Surface Waves, *Surv. Geophys.*, *30*(4-5), 463–501, doi:10.1007/s10712-009-9066-2.

Boschi, L., C. Faccenna, and T. W. Becker (2010), Mantle structure and dynamic topography in the Mediterranean Basin, *Geophys. Res. Lett.*, *37*(20), 1–6, doi:10.1029/2010GL045001.

Boschi, L., C. Weemstra, J. Verbeke, G. Ekström, and D. Giardini (2012), On measuring surface-wave phase velocity from station-station cross-correlation of ambient signal., *submitted to Geophys. J. Int.*

Campillo, M., and A. Paul (2003), Long-range correlations in the diffuse seismic coda, *Science*, *299*(5606), 547–549, doi:10.1126/science.1078551.

Chang, S.-J., et al. (2010), Joint inversion for three-dimensional S velocity mantle structure along the Tethyan margin, *J. Geophys. Res.*, *115*(B8), 1–22, doi:10.1029/2009JB007204.

Cox, H. (1973), Spatial correlation in arbitrary noise fields with application to ambient sea noise, *J. Acoust. Soc. Am.*, *54*(5), 1289–1301.

Dahlen, F., and J. Tromp (1998), *Theoretical Global Seismology*, Princeton University Press.

Duvall, T., S. Jeffferies, J. Harvey, and M. Pomerantz (1993), Timedistance helioseismology, *Nature*, *362*(6419), 430–432.

Grad, M., and T. Tiira (2009), The Moho depth map of the European Plate, *Geophys. J. Int.*, *176*(1), 279–292, doi:10.1111/j.1365-246X.2008.03919.x.

693 Hanasoge, S. (2012), The influence of noise sources on cross-correlation amplitudes, *Geo-*
694 *phys. J. Int.*, *submitted*.

695 Hasselmann, K. (1963), A statistical analysis of the generation of microseisms, *Rev. Geo-*
696 *phys.*, *1*(2), 177–210, doi:10.1029/RG001i002p00177.

697 Hillers, G., N. Graham, M. Campillo, S. Kedar, M. Landès, and N. Shapiro (2012),
698 Global oceanic microseism sources as seen by seismic arrays and predicted by wave
699 action models, *Geochem. Geophy. Geosy.*, *13*(1), Q01021, doi:10.1029/2011GC003875.

700 Karato, S. (2003), *The dynamic structure of the deep Earth*, Princeton University Press.

701 Kedar, S., M. Longuet-Higgins, F. Webb, N. Graham, R. Clayton, and C. Jones (2008),
702 The origin of deep ocean microseisms in the North Atlantic Ocean, *Proc. R. Soc. A*,
703 *464*, 777–793, doi:10.1098/rspa.2007.0277.

704 Landès, M., F. Hubans, N. M. Shapiro, A. Paul, and M. Campillo (2010), Origin of deep
705 ocean microseisms by using teleseismic body waves, *J. Geophys. Res.*, *115*, B05302,
706 doi:10.1029/2009JB006918.

707 Longuet-Higgins, M. S. (1950), A theory of the origin of microseisms, *Phil. Trans. R. Soc.*
708 *A*, *243*, 1–35.

709 Mikesell, T. D., K. van Wijk, T. E. Blum, R. Snieder, and H. Sato (2012), Analyzing the
710 coda from correlating scattered surface waves., *J. Acoust. Soc. Am.*, *131*(3), EL275–81,
711 doi:10.1121/1.3687427.

712 Molinari, I., and A. Morelli (2011), EPcrust: a reference crustal model for the European
713 Plate, *Geophys. J. Int.*, *185*(1), 352–364, doi:10.1111/j.1365-246X.2011.04940.x.

714 Molinari, I., J. Verbeke, L. Boschi, E. Kissling, and A. Morelli (2012), Mapping the
715 Italian and Central Europe crust from a combination of ambient-noise and seismic

716 data, *Geochem. Geophy. Geosy.*, *submitted*.

717 Mulargia, F. (2012), The seismic noise wavefield is not diffuse., *J. Acoust. Soc. Am.*,
718 *131*(4), 2853–8, doi:10.1121/1.3689551.

719 Paul, A., M. Campillo, L. Margerin, E. Larose, and A. Derode (2005), Empirical synthesis
720 of time-asymmetrical Green function from the correlation of coda waves, *J. Geophys.*
721 *Res.*, *110*, B08302, doi:10.1029/2004JB003521.

722 Peter, D., C. Tape, L. Boschi, and J. H. Woodhouse (2007), Surface wave tomography:
723 global membrane waves and adjoint methods, *Geophys. J. Int.*, *171*(3), 1098–1117,
724 doi:10.1111/j.1365-246X.2007.03554.x.

725 Peter, D., et al. (2011), Forward and adjoint simulations of seismic wave propagation
726 on fully unstructured hexahedral meshes, *Geophys. J. Int.*, *186*(2), 721–739, doi:
727 10.1111/j.1365-246X.2011.05044.x.

728 Peterson, J. (1993), Observations and modelling of background seismic noise.

729 Sabra, K. G., P. Gerstoft, P. Roux, W. A. Kuperman, and M. C. Fehler (2005), Surface
730 wave tomography from microseisms in Southern California, *Geophys. Res. Lett.*, *32*,
731 L14311, doi:10.1029/2005GL023155.

732 Schaefer, J. F., L. Boschi, T. W. Becker, and E. Kissling (2011), Radial anisotropy in
733 the European mantle: Tomographic studies explored in terms of mantle flow, *Geophys.*
734 *Res. Lett.*, *38*(23), 1–5, doi:10.1029/2011GL049687.

735 Schivardi, R., and A. Morelli (2009), Surface wave tomography in the European
736 and Mediterranean region, *Geophys. J. Int.*, *177*(3), 1050–1066, doi:10.1111/j.1365-
737 246X.2009.04100.x.

738 Schmid, C., S. van der Lee, and D. Giardini (2004), Delay times and shear wave splitting
739 in the Mediterranean region, *Geophys. J. Int.*, *159*(1), 275–290.

740 Shapiro, N. M., and M. Campillo (2004), Emergence of broadband Rayleigh waves
741 from correlations of the seismic ambient noise, *Geophys. Res. Lett.*, *31*, L07614, doi:
742 10.1029/2004GL019491.

743 Shapiro, N. M., M. Campillo, L. Stehly, and M. H. Ritzwoller (2005), High-resolution
744 surface-wave tomography from ambient seismic noise., *Science*, *307*(5715), 1615–8, doi:
745 10.1126/science.1108339.

746 Snieder, R. (2004), Extracting the Greens function from the correlation of coda
747 waves: A derivation based on stationary phase, *Phys. Rev. E*, *69*(4), doi:
748 10.1103/PhysRevE.69.046610.

749 Stehly, L., M. Campillo, and N. M. Shapiro (2006), A study of the seismic noise
750 from its long-range correlation properties, *J. Geophys. Res.*, *111*(B10), 1–12, doi:
751 10.1029/2005JB004237.

752 Stehly, L., B. Fry, M. Campillo, N. M. Shapiro, J. Guilbert, L. Boschi, and D. Giardini
753 (2009), Tomography of the Alpine region from observations of seismic ambient noise,
754 *Geophys. J. Int.*, *178*(1), 338–350, doi:10.1111/j.1365-246X.2009.04132.x.

755 Tanimoto, T. (2008), Normal-mode solution for the seismic noise cross-correlation method,
756 *Geophys. J. Int.*, *175*(3), 1169–1175, doi:10.1111/j.1365-246X.2008.03959.x.

757 Tape, C., Q. Liu, and J. Tromp (2007), Finite-frequency tomography using adjoint
758 methods-Methodology and examples using membrane surface waves, *Geophys. J. Int.*,
759 *168*(3), 1105–1129, doi:10.1111/j.1365-246X.2006.03191.x.

760 Tape, C., Q. Liu, A. Maggi, and J. Tromp (2010), Seismic tomography of the south-
761 ern California crust based on spectral-element and adjoint methods, *Geophys. J. Int.*,
762 *180*(1), 433–462, doi:10.1111/j.1365-246X.2009.04429.x.

763 Tesauro, M., M. K. Kaban, and S. A. P. L. Cloetingh (2008), EuCRUST-07: A
764 new reference model for the European crust, *Geophys. Res. Lett.*, *35*(5), 1–5, doi:
765 10.1029/2007GL032244.

766 Tromp, J., C. Tape, and Q. Liu (2005), Seismic tomography, adjoint methods, time rever-
767 sal and banana-doughnut kernels, *Geophys. J. Int.*, *160*(1), 195–216, doi:10.1111/j.1365-
768 246X.2004.02453.x.

769 Tromp, J., D. Komattisch, and Q. Liu (2008), Spectral-element and adjoint methods in
770 seismology, *Commun. Comput. Phys.*, *3*(1), 1–32.

771 Tromp, J., Y. Luo, S. Hanasoge, and D. Peter (2010), Noise cross-correlation sensitivity
772 kernels, *Geophys. J. Int.*, *183*(2), 791–819, doi:10.1111/j.1365-246X.2010.04721.x.

773 Tsai, V. C., and M. P. Moschetti (2010), An explicit relationship between time-domain
774 noise correlation and spatial autocorrelation (SPAC) results, *Geophys. J. Int.*, *182*(1),
775 454–460, doi:10.1111/j.1365-246X.2010.04633.x.

776 Verbeke, J., L. Boschi, L. Stehly, E. Kissling, and a. Michelini (2012), High-resolution
777 Rayleigh-wave velocity maps of central Europe from a dense ambient-noise data set,
778 *Geophys. J. Int.*, *188*(3), 1173–1187, doi:10.1111/j.1365-246X.2011.05308.x.

779 Yang, Y., M. H. Ritzwoller, F.-C. Lin, M. P. Moschetti, and N. M. Shapiro (2008),
780 Structure of the crust and uppermost mantle beneath the western United States revealed
781 by ambient noise and earthquake tomography, *J. Geophys. Res.*, *113*(B12), 1–9, doi:
782 10.1029/2008JB005833.

Zhou, Y., Q. Liu, and J. Tromp (2011), Surface wave sensitivity: mode summation versus adjoint SEM, *Geophys. J. Int.*, *187*(3), 1560–1576, doi:10.1111/j.1365-246X.2011.05212.x.

Zhu, H., E. Bozda, D. Peter, and J. Tromp (2012), Structure of the European upper mantle revealed by adjoint tomography, *Nature Geosci.*, *5*(7), 493–498, doi:10.1038/ngeo1501.

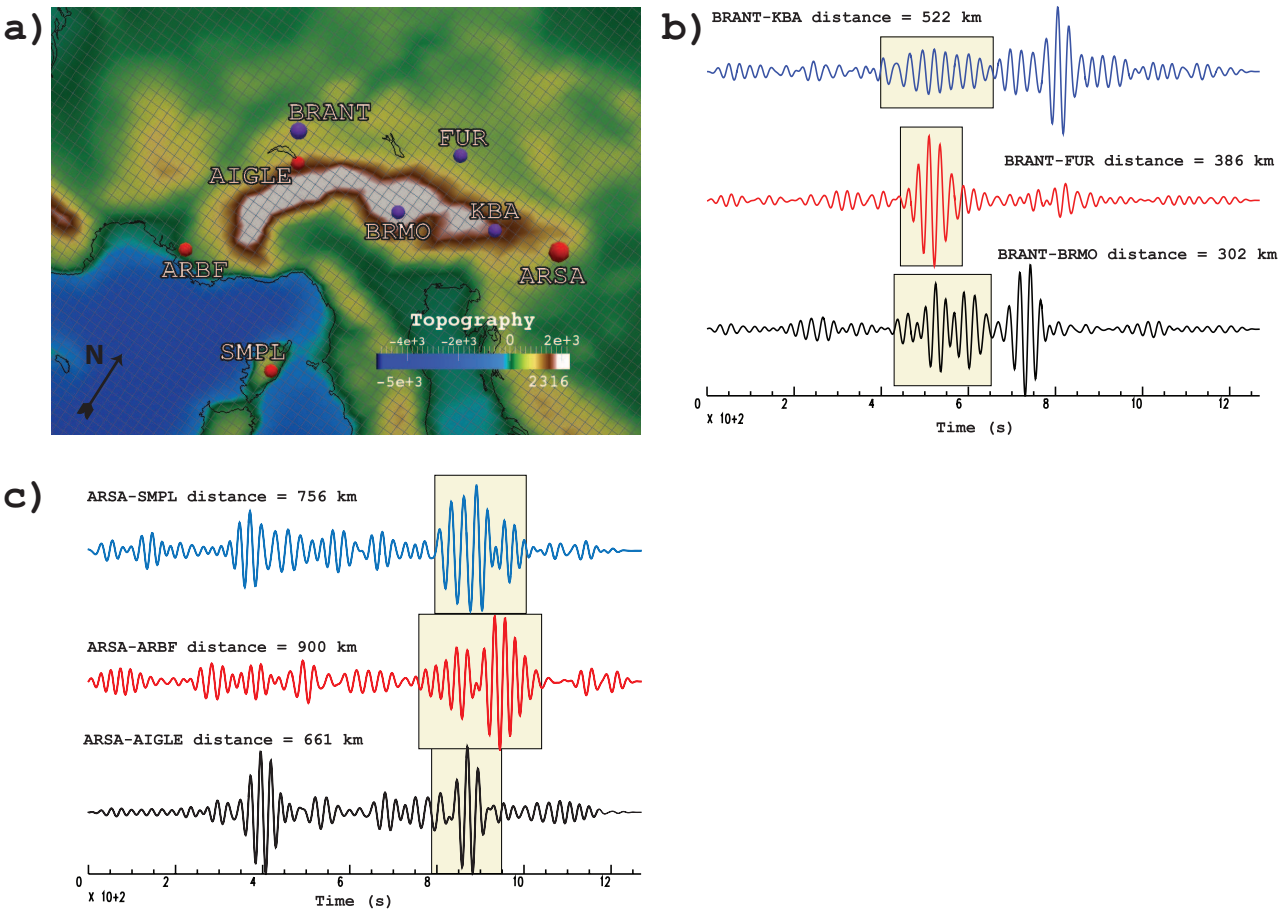

Figure 1. Set of correlograms (vertical components) from ambient noise recorded data, showing a certain portion of energy coming from east, all correlograms have been normalized to the unit so the vertical axis is not shown. (a) Positions of two sets (red dots and purple dots) of seismic stations. (b) Each time series represents a observation-based ambient noise correlogram with BRANT as reference station, the other stations used are respectively KBA (blue line), FUR (red line) and BRMO (black line). Since the reference station is located westward with respect to the others (panel (a)), surface waves traveling from east are visible in the left part, the anticausal one, of these correlograms. (c) In this case the reference station is ARSA and the one used to compute the correlograms are SMPL (blue line), ARBF (red line) and AIGLE (black line). The reference station is positioned eastward with respect to the others (panel (a)), thus it is possible to recognize the energy of surface waves propagating from east in the shaded boxes in the right part of the correlograms. Data in panel (b) and (c) are filtered using a bandpass Butterworth filter between 20 and 30 s.

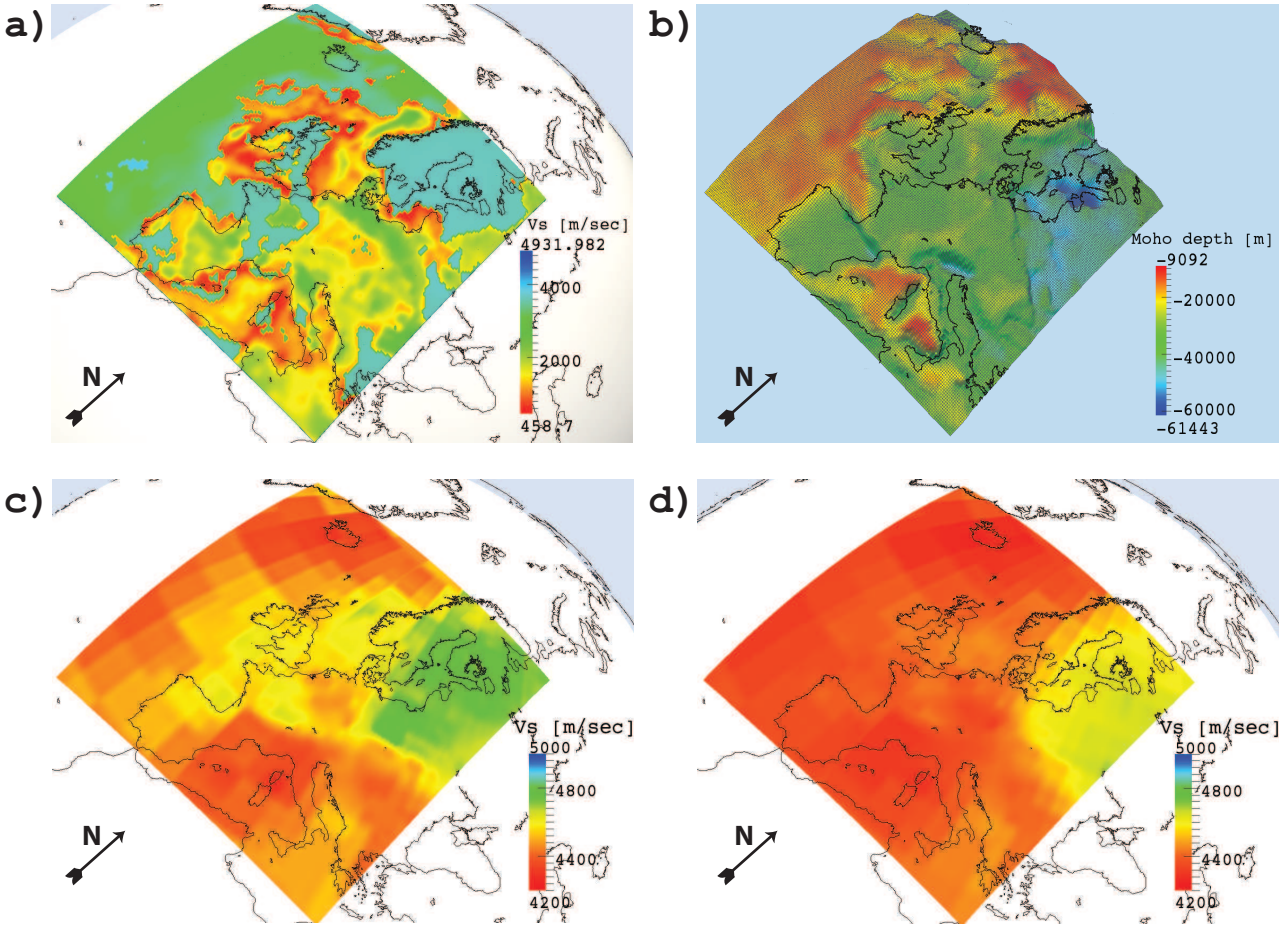

Figure 2. (a) Map for shear waves speed values of model EPcrust just below the free surface. Low velocity values are typical of sedimentary basins. Observed contrasts in speed values are caused by the absence of sediments in certain areas of our study region. (b) 3D view of the Moho surface geometry using an exaggeration factor of 10 to enhance the perspective. (c) Map for shear waves speed values of model FMADVOXEU′ at a depth of 78 km. (d) Map for shear waves speed values of model FMADVOXEU′ at a depth of 128 km.

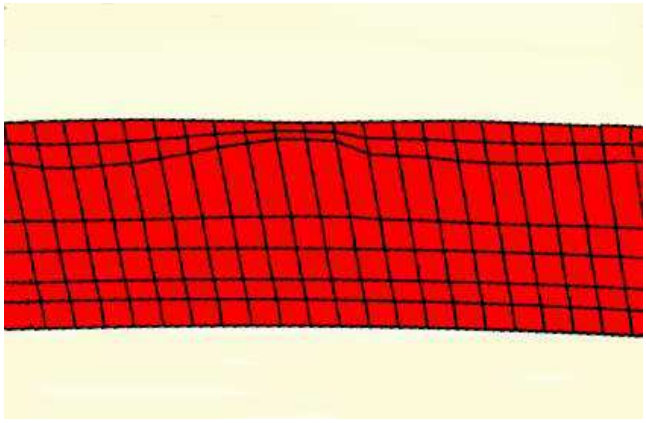

Figure 3. Close view of a vertical cross-section of the mesh used in this work. Topography is present but not visible at this one-to-one scale. The crustal layer is reproduced by means of two spectral elements. Notice how the irregular shape of the Moho produces a strong squeezing of the elements. This factor drives the stability condition of our simulations.

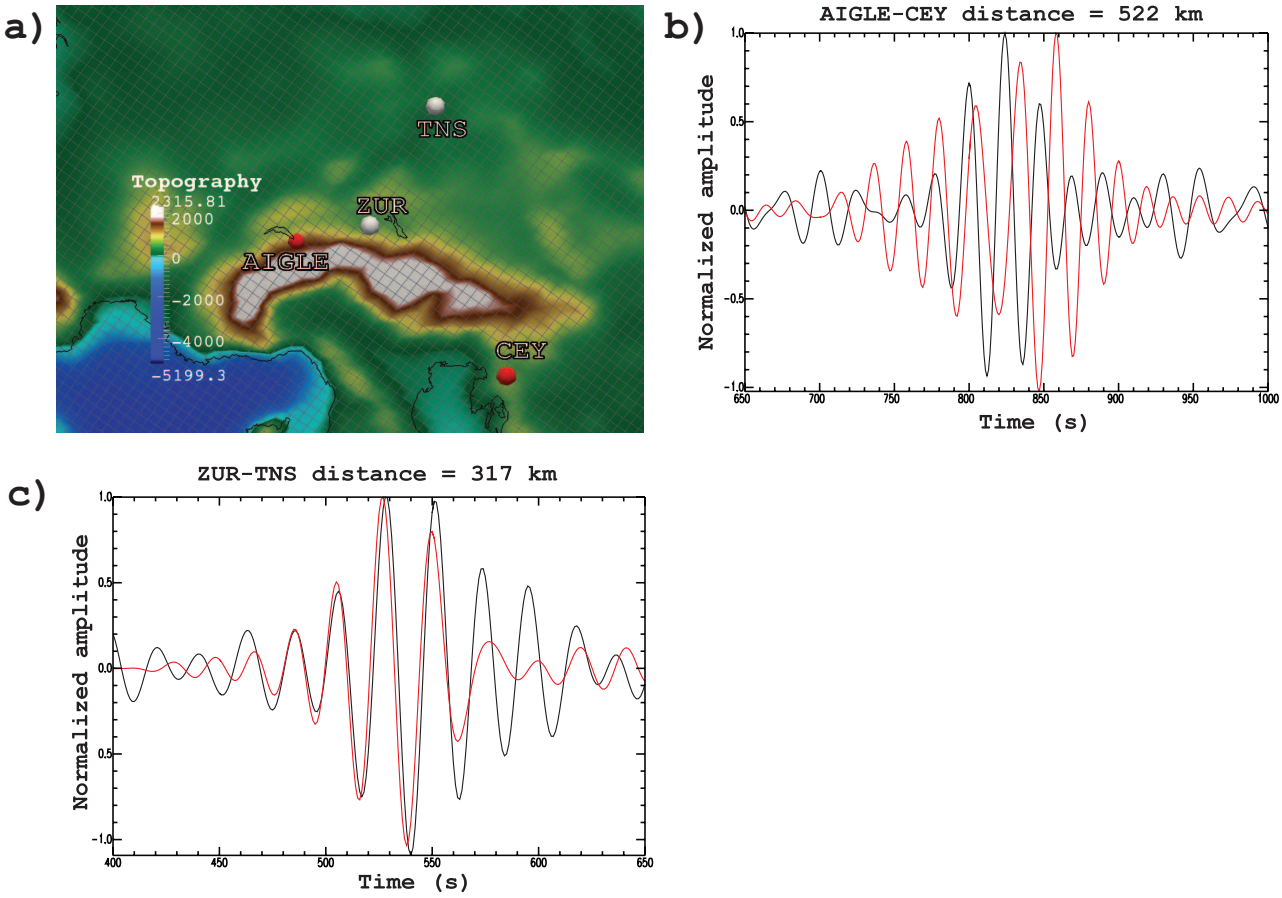

Figure 4. (a) Position of the two station couples. (b) and (c) comparison between correlograms from observation-based (black line) and synthetic (red line) traces. The unacceptable misfit between data and synthetic in panel (b) indicates how the model we used does not describe the complexity of the Alpine region very well. Synthetic correlograms are obtained following the methodology described in Section 4 and outlined in figure 5.

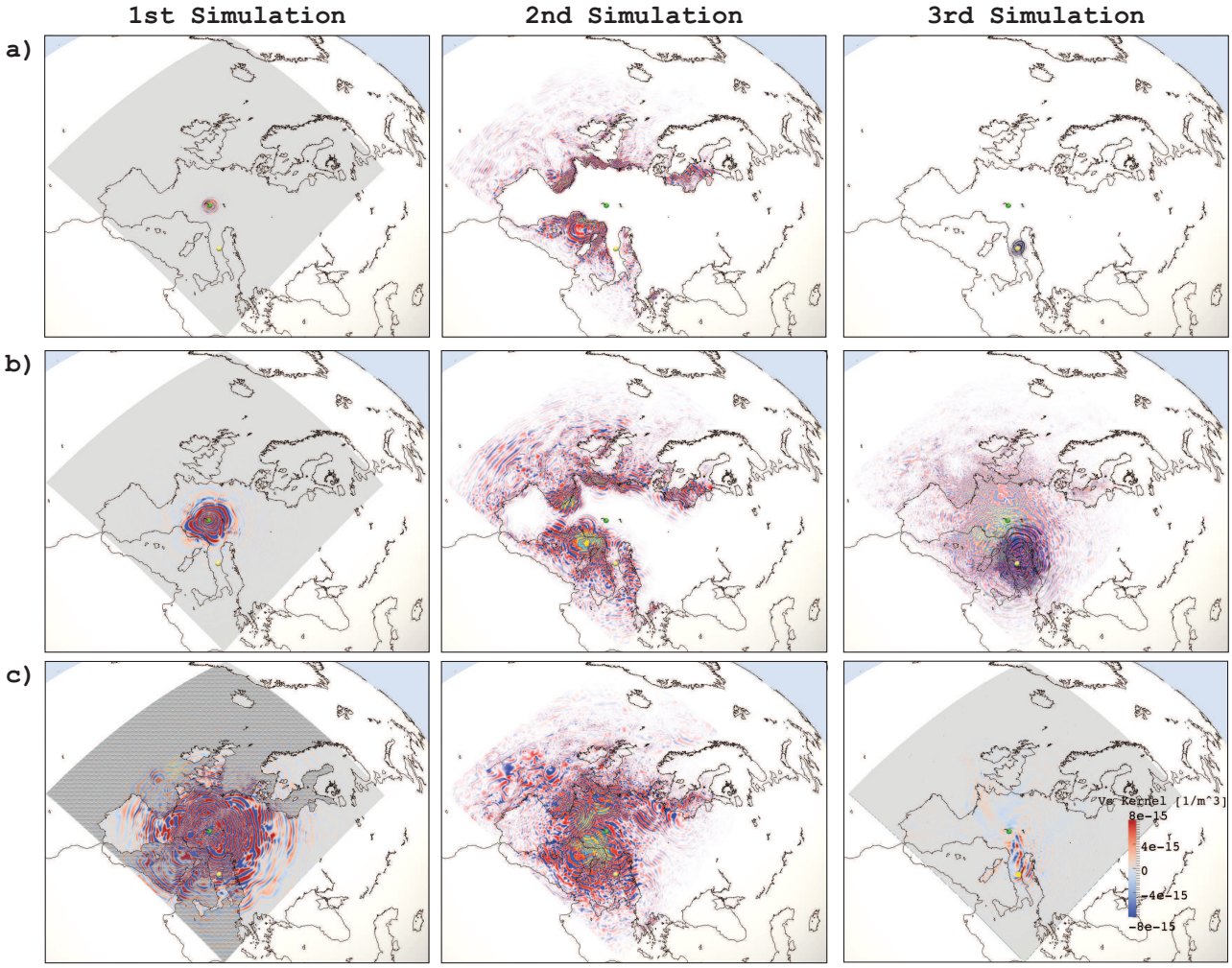

Figure 5. Synoptic scheme of the three simulations described in Section 4. Each column reproduces the subsequent steps of a simulation. The green dot represents the reference station AIGLE (station α in Section 4), while station AQU (station β in Section 4) is indicated by the yellow dot. First column: three snapshots of the wavefield of the first simulation, produced by the forcing term F_i^α defined in equation (A12). Dark grey dotted area in the bottom left panel indicates the region where we guess all the noise sources are located and where the wavefield of the first simulation is stored. Second column: three snapshot of the second simulation where the wavefield stored from column (1) is used as forcing term and the result is the wavefield $\mathbf{\Phi}^\alpha(\mathbf{x},\omega)$ of equation (A14). Third column (a)-(b): adjoint wavefield driven by eq.(4) and its interaction with the reconstructed field of the second simulation. Bottom right panel: picture of the "causal" β sensitivity kernel eq. (5).

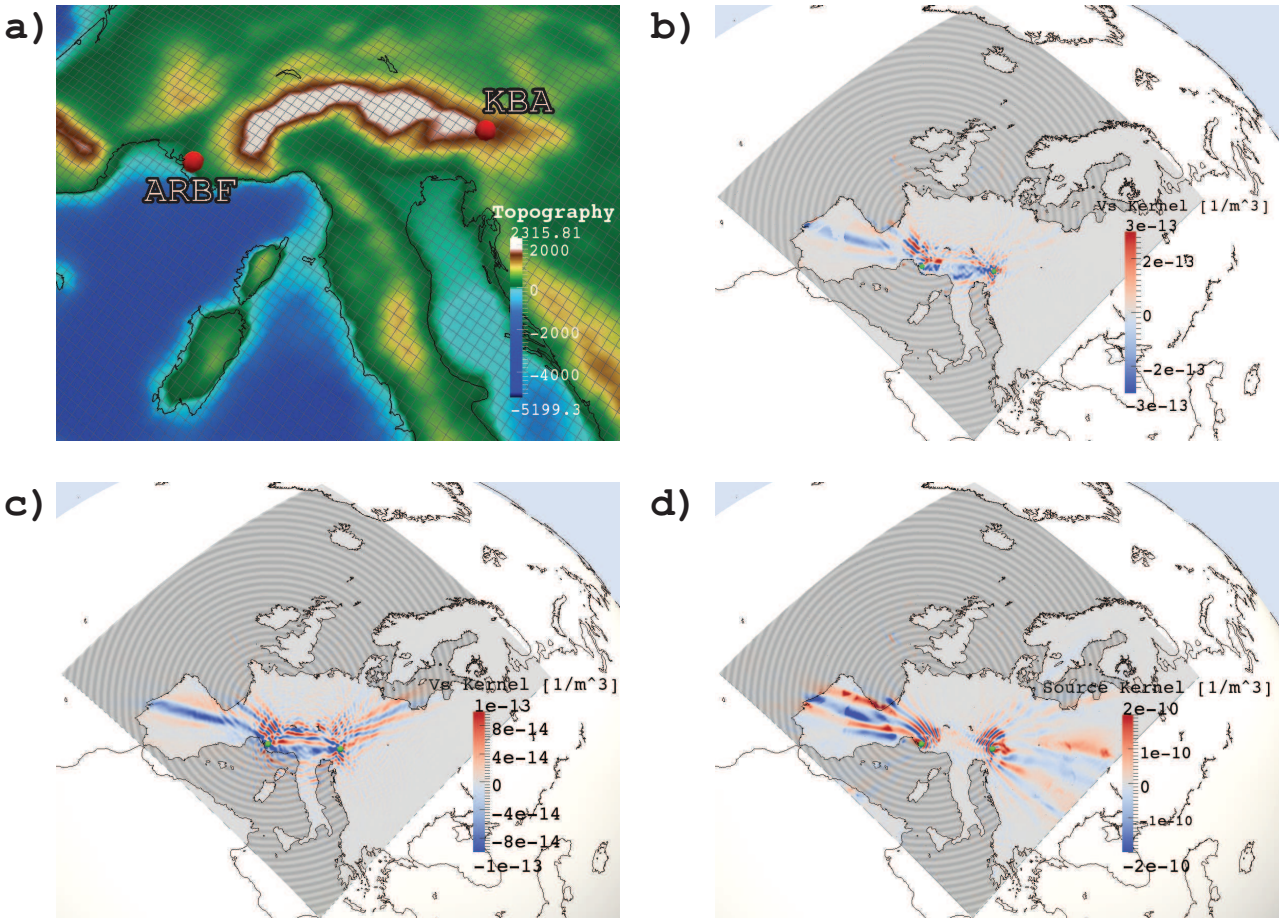

Figure 6. Demonstrating the effect of uniform ocean noise sources, represented by the grey circles, on the β and source sensitivity kernels. (a) Locations of stations ARBF (left red dot) and KBA (right red dot). (b) Shear wavespeed kernel for station pair ARBF-KBA just below the free surface. Sensitivity extends also outside the region between the two stations: this behavior is caused by the non uniform distribution of noise sources. (c) Same kernel showed in panel (b), but at a depth of 30 km. Owing to the absence of sediments at this depth, the kernel is smoother. (d) Source kernel. The two areas of sensitivity centered onto the seismic stations have interesting features: (i) the one pointing westward shows higher values than the one pointing eastward, and (ii) it has not the same hyperbolic shape of the one centered on KBA (sensitivity in the Mediterranean is near zero). These features indicate that most of the energy originates in the Atlantic.

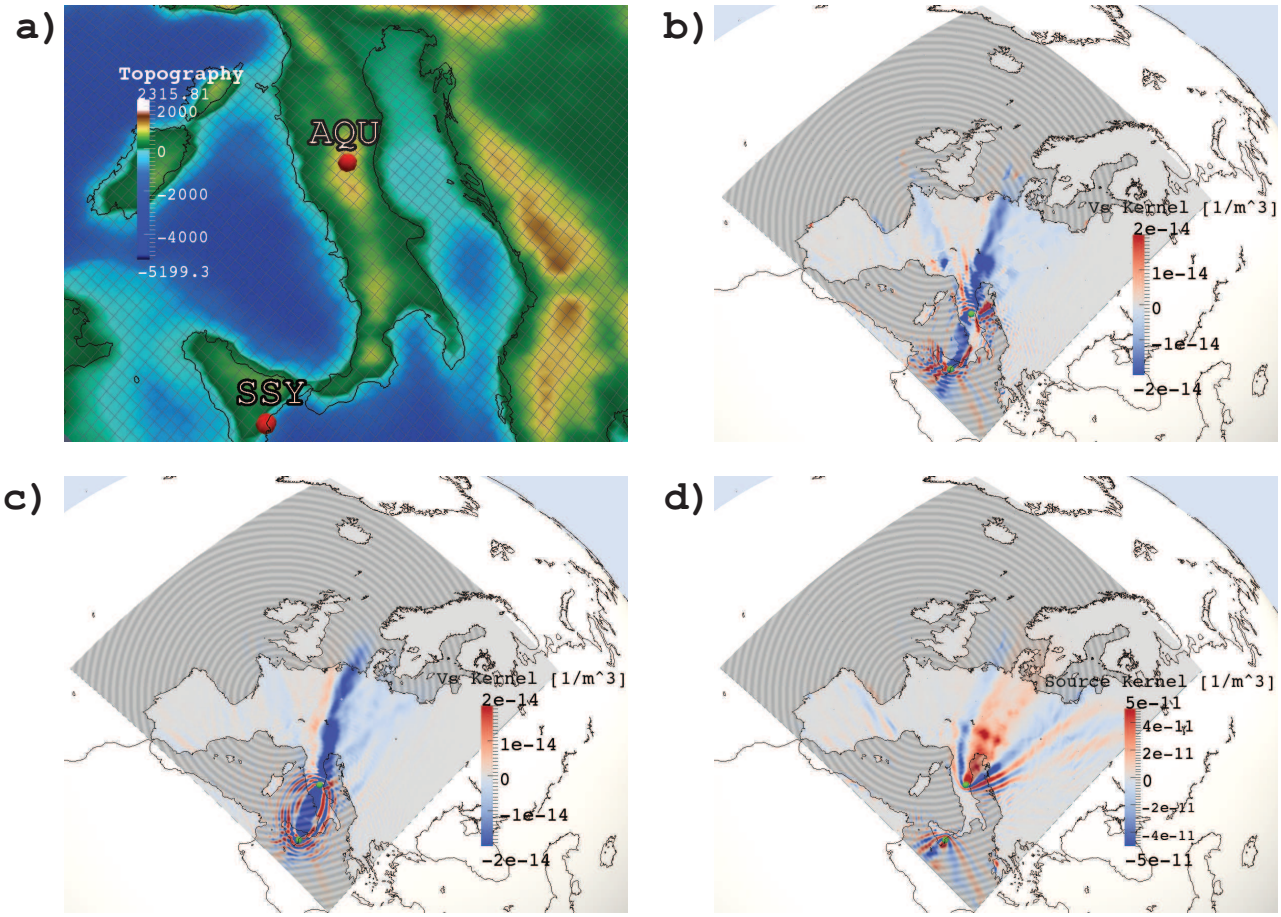

Figure 7. (a) Locations of stations AQU (center Italy) and SSY (Sicily). Synthetic ambient noise sources are placed in all seas and are represented by the grey circles. (b)K_β for station-pair AQU-SSY just below the free surface. The sensitivity is concentrated between the two stations and in a small area around them with three "jets" departing from station AQU: the first one points towards the Alpine region while the other two are directed towards Croatia. (c) Slice of K_β taken at a depth of 30 Km. Considerations made for panel (c) in figure 6 are also valid in this case. (d) The high symmetry shown by K_σ is caused by the north-south orientation of the stations pair: synthetic ambient noise comes from the north (North Sea) as well from the south (Mediterranean), thus this situation is similar to a uniform distribution of noise sources.

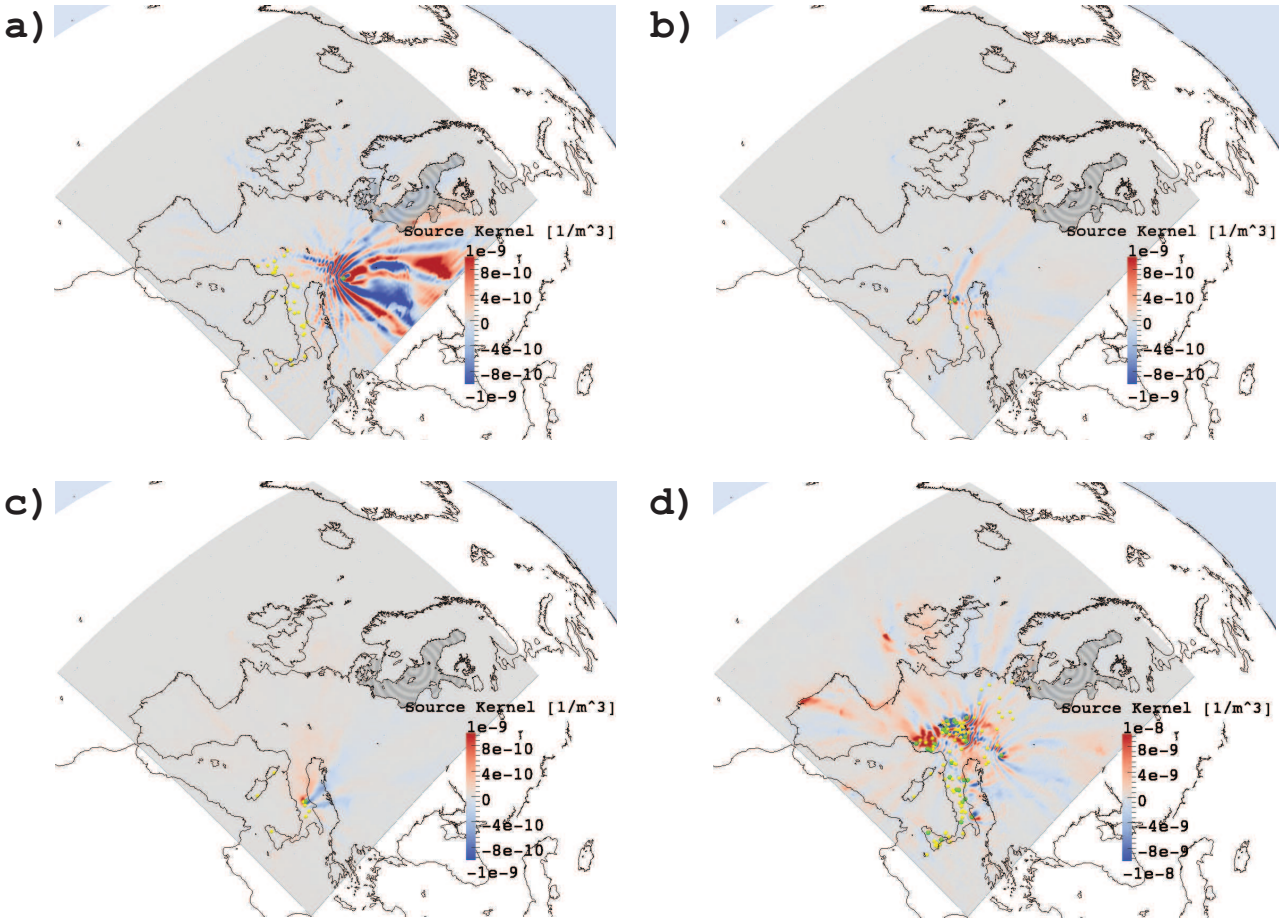

Figure 8. Source sensitivity kernels, K_σ, for noise sources from the Baltic Sea, denoted by grey circles. (a) K_σ for reference seismic station ARSA (green dot). It was possible to define an higher number of adjoint source, yellow dots, than in the case for reference stations ARCI and BSSO, respectively panels (b) and (c). The high sensitivity area in the eastern part of the region can not be simply associated with the geographical position of station ARSA with respect to the others, as we can see from figure 9. (b) K_σ for reference seismic station ARCI (green dot). (c) K_σ for reference seismic station BSSO (green dot). (d) K_σ kernel obtained as the sum over 26 reference-station kernels. There are three main lobes pointing towards three different region: the Mediterranean Sea, the Atlantic Ocean, and the eastern part of the study area.

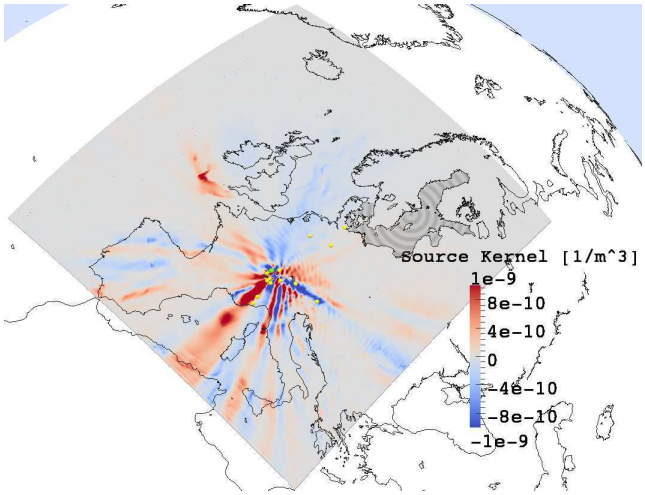

Figure 9. K_σ for reference seismic station BRANT (green dot). Noise sources are located only in the Baltic Sea and are denoted by grey circles. Even if the geographical position of the reference station with respect to the others suggests the sensitivity to be concentrated in the western part of the study area, it is possible to see a strong "jet" of sensitivity protruding eastwards.

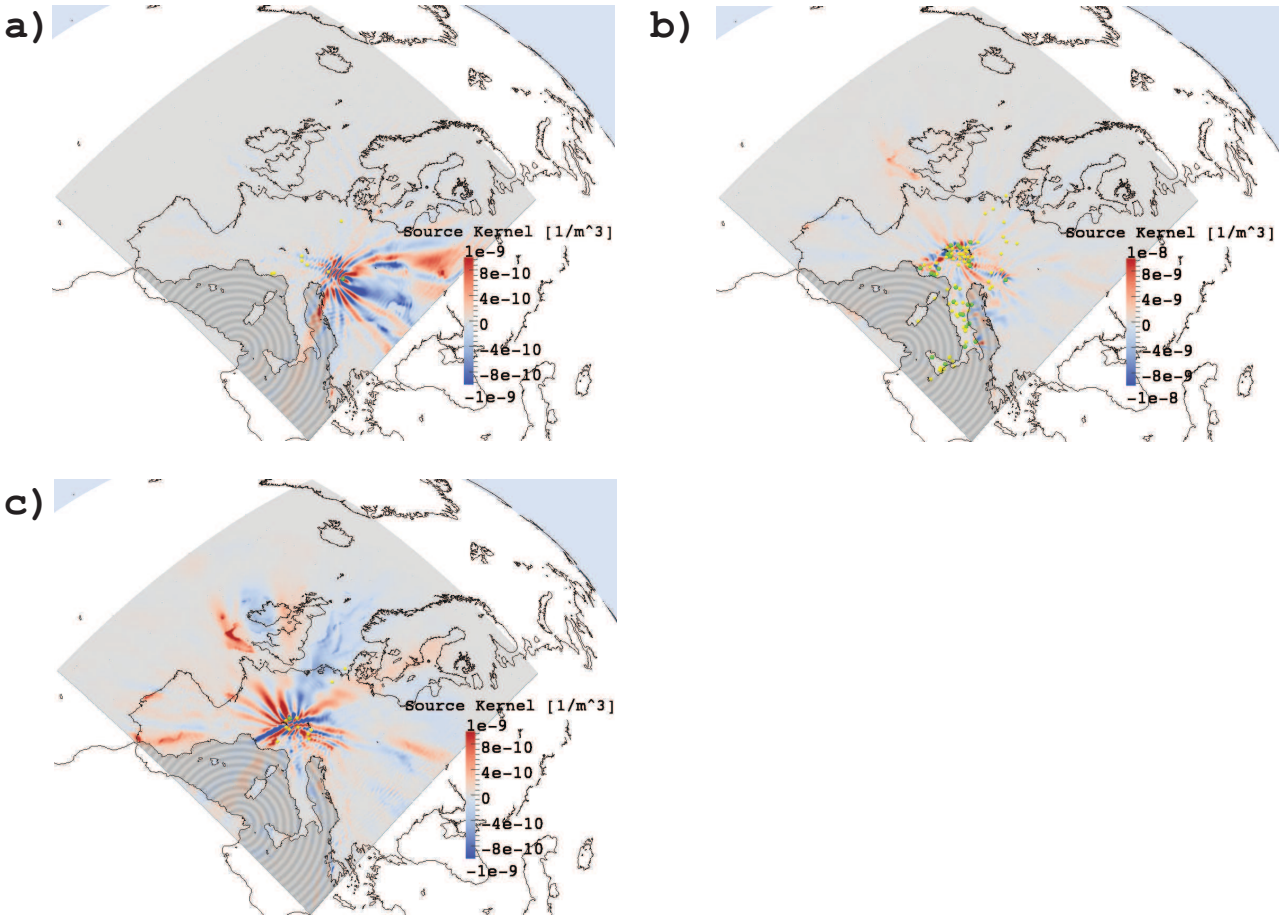

Figure 10. Source sensitivity kernels, K_σ, for noise sources from the Mediterranean Sea, represented by grey circles. (a) K_σ computed for reference station ARSA (green dot). The stations used to construct the sensitivity kernel, yellow dots, are different from the ones used in figure 8: if we do not consider ambient noise coming from the Baltic region then the misfit between synthetic and observation-based correlograms exceed the limit we impose to build the adjoint sources. However the sensitivity is still concentrated in the eastern region. (b) Source kernel obtained as the sum of 26 single contributions and for a distribution of sources concentrated only in the Mediterranean Sea. The comparison with figure 8 panel (d) shows how sensitivity towards both the Atlantic and the Mediterranean decreases remarkably. However it is still possible to observe some sensitivity in the eastern region. (c) K_σ computed for reference station BRANT (green dot).

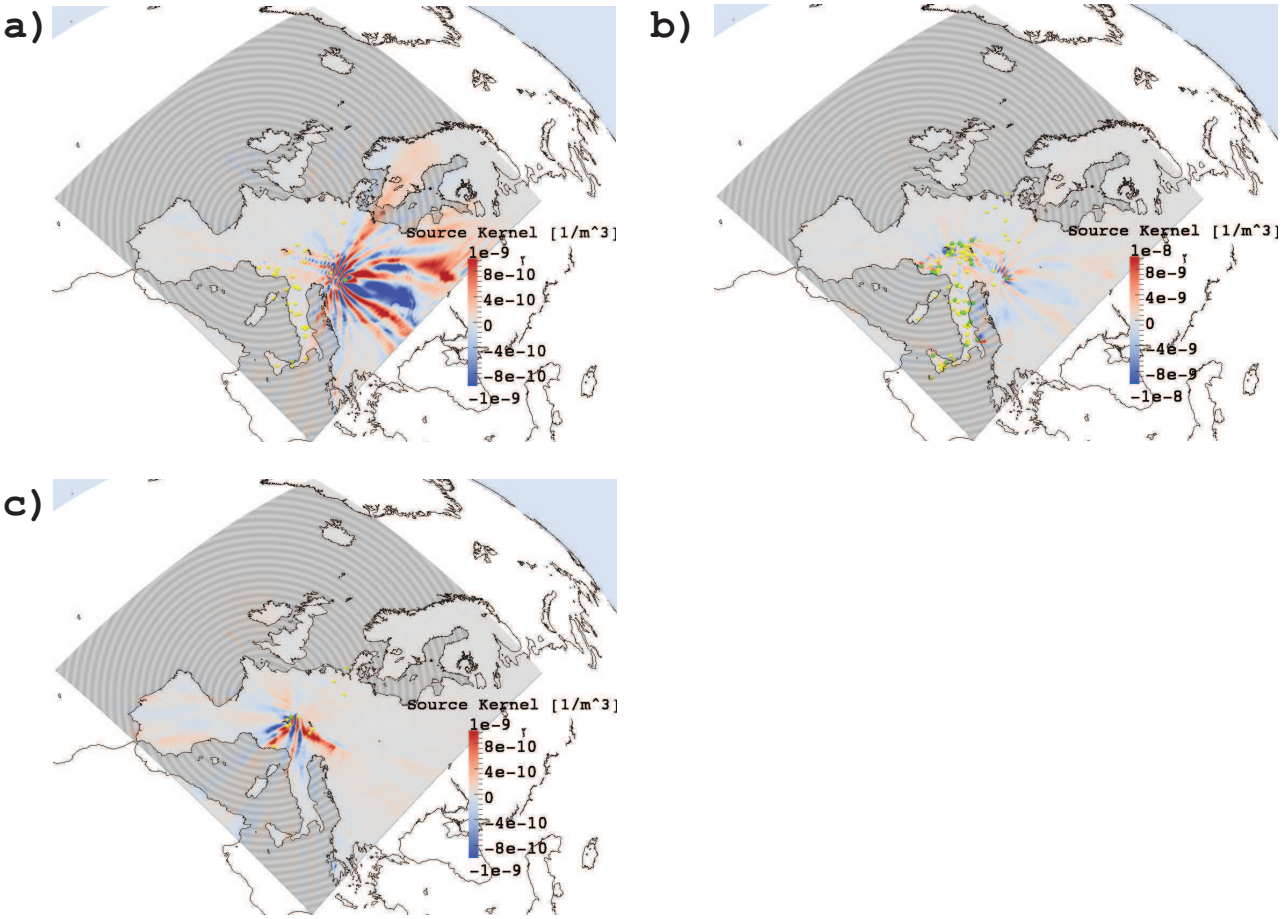

Figure 11. (a) K_σ computed for reference station ARSA (green dot) and noise sources, denoted by grey circles, located in all the sea regions. For this figure are valid the same considerations we did in figure 8 panel (a). (b) K_σ obtained as the sum of 26 single contributions and for a distribution of sources distributed throughout all sea regions. The sensitivity area near the Atlantic and the one in the Mediterranean are almost reduced to zero. It is still possible to observe lobes of sensitivity pointing towards east. (c) K_σ computed for reference station BRANT (green dot) and noise sources located in all the sea regions.

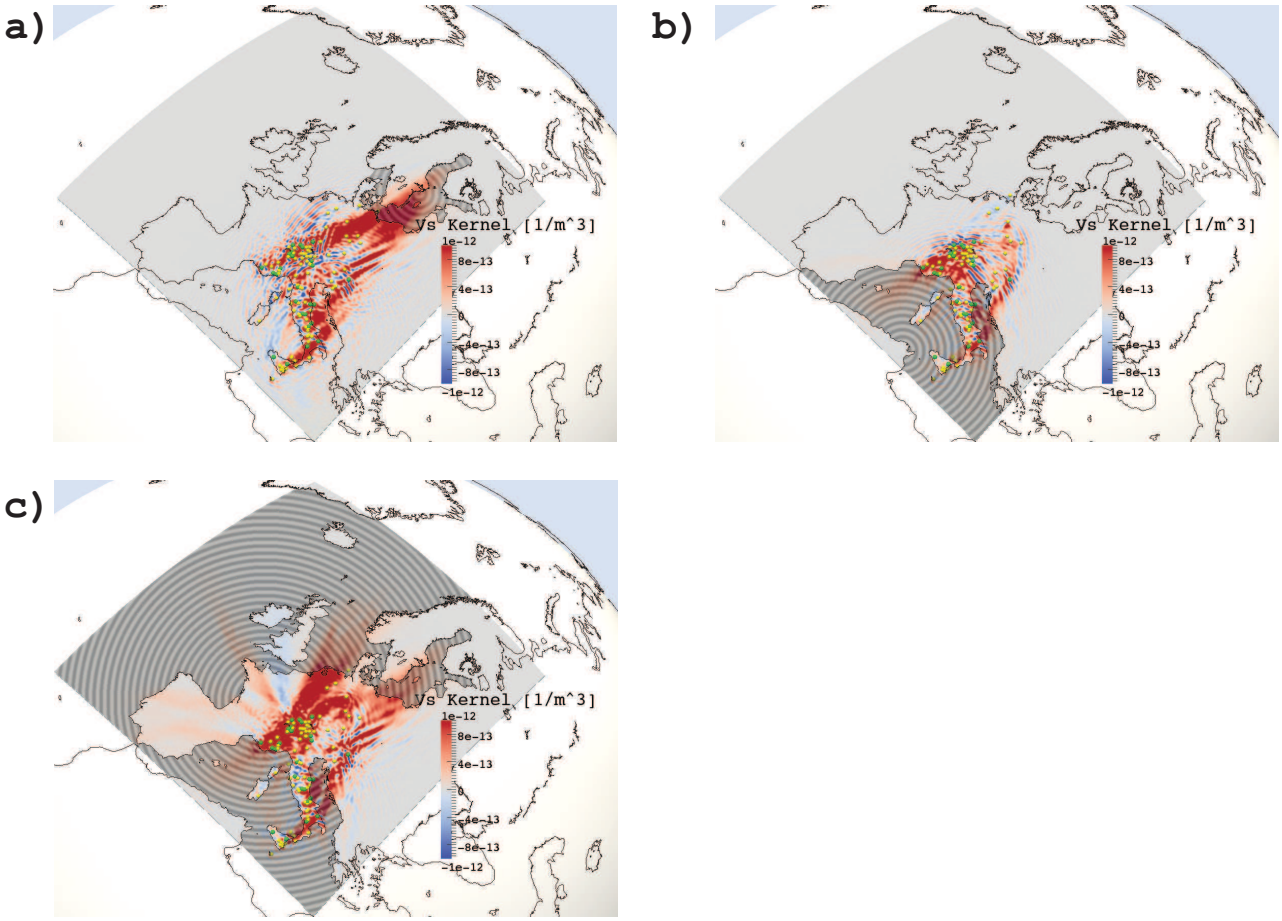

Figure 12. K_β kernel obtained as the sum of 26 different contributions for three different distributions of noise sources, represented by grey circles in the pictures: noise sources distributed in the Baltic Sea, panel (a), in the Mediterranean, panel (b), and in all the sea regions, panel (c). All the kernels are taken at a depth of 30 km. Sensitivity is characterized by positive values in all three cases, indicating that our 3D shear background model is too slow. Areas illuminated by the sensitivity drastically change when we consider different distributions of noise sources: in panel (b) there is no sign of sensitivity in the area of the Baltic Sea, and both panel (a) and (b) do not show any sensitivity in France or Spain, as happens in panel (c) instead.

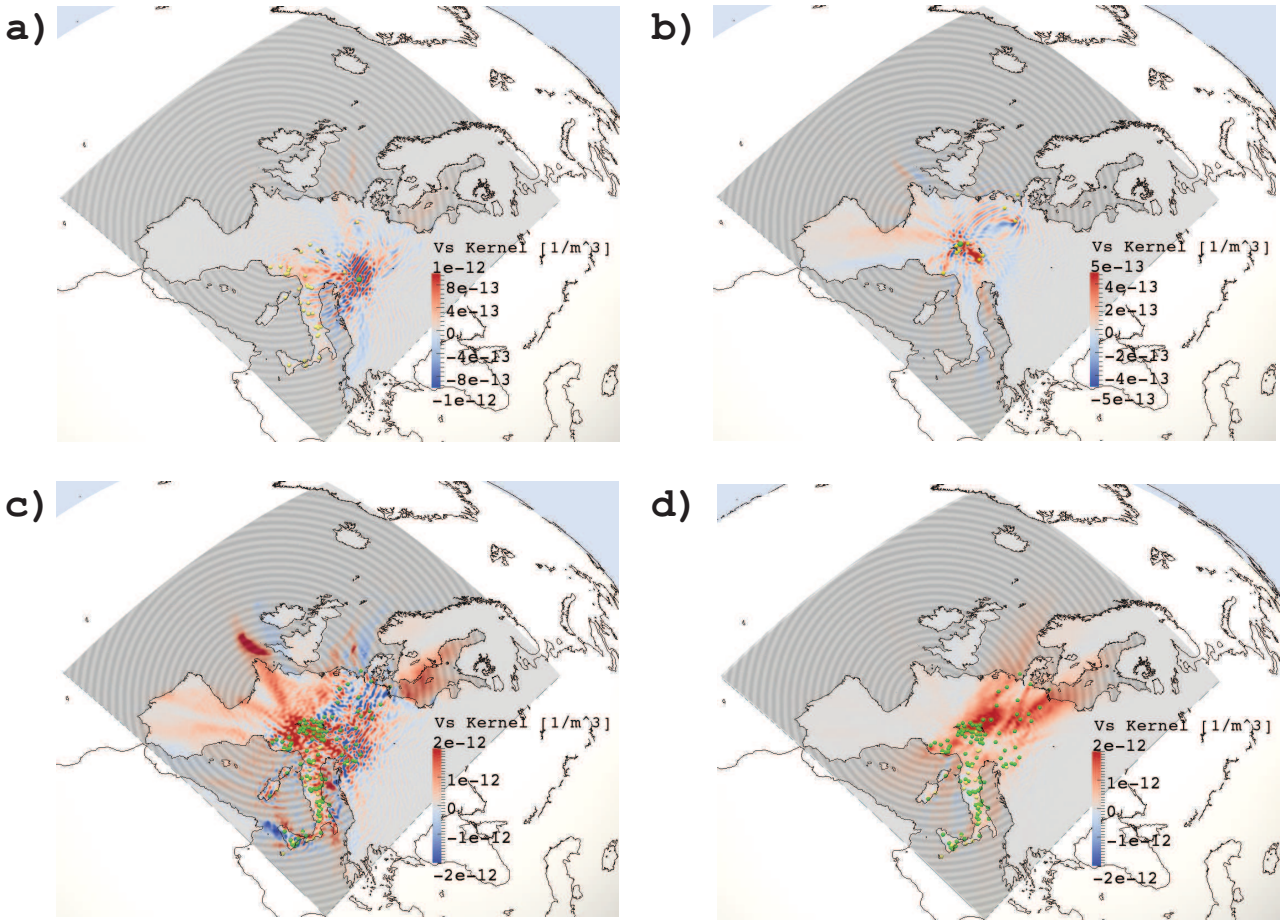

Figure 13. Structure sensitivity kernels, K_β, for noise sources located in all the sea regions, denoted by grey circles. Panels (a) and (b): slice of K_β computed respectively for reference station ARSA and BRANT (green dots) taken at a depth of 10 km. Panel (a) presents higher values of sensitivity with respect to panel (b) as happened in the case of K_σ, this will influence also the shape and values of the misfit kernel. Panels (c) and (d): slices of K_β kernel taken respectively at 10 and 70 km. The kernel is obtained as the sum of 104 different contributions. At 10 km depth Alpine region shows strong positive sensitivity, areas with negative values are concentrated mainly in the northeast part of the study region. At 70 km depth the sensitivity is almost completely positive indicating how the model we used has to be corrected with higher values of β.

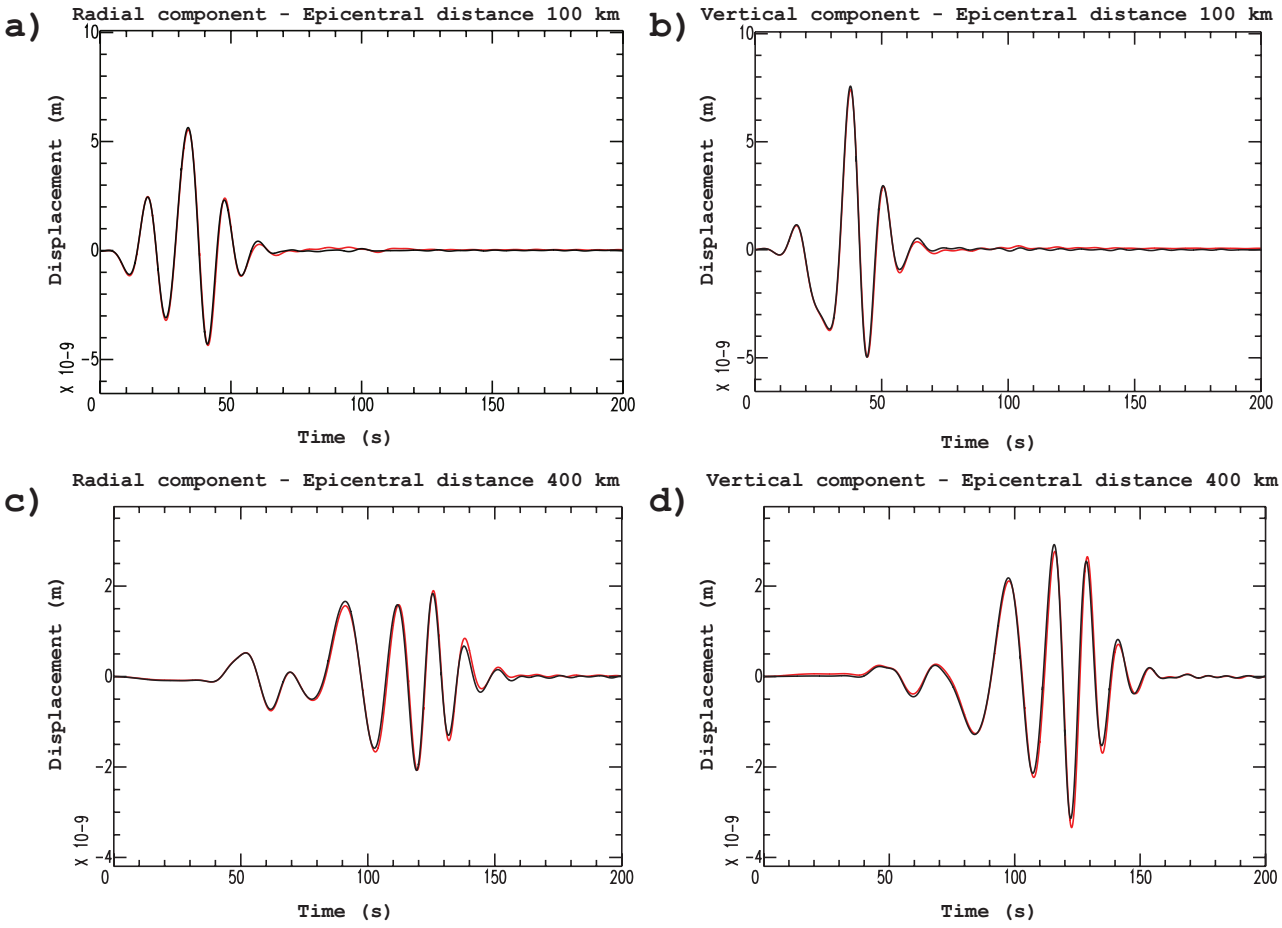

Figure 14. Results for the benchmark test between SPECFEM3D version 2.0, red lines, and SPECFEM3D_GLOBE, black lines. We placed a cross-shaped array of seismic receivers with interstation distance of about 100 km and we simulated a 10 km deep explosion at the center of the array. We applied a bandpass Butterworth filter between 10 and 30 s. We have omitted the transverse components which are zero.